ISWI catalyzes nucleosome sliding in condensed nucleosome arrays

Authors

Petra Vizjak[1,3], Dieter Kamp[2], Nicola Hepp[3,9,*], Alessandro Scacchetti[3,8,*], Mariano Gonzalez Pisfil[4], Joseph Bartho[2], Mario Halic[5], Peter B. Becker[3], Michaela Smolle[6,7], Johannes Stigler[2,#], Felix Mueller-Planitz[1,#]

Affiliations

1 Institute of Physiological Chemistry, Faculty of Medicine Carl Gustav Carus, Technische Universität Dresden, Fetscherstraße 74, 01307 Dresden, Germany

2 Gene Center, Department of Biochemistry, Ludwig-Maximilians-Universität München, Feodor-Lynen-Str 25, 81377 München, Germany

3 Department of Molecular Biology, Biomedical Center, Faculty of Medicine, Ludwig-Maximilians-Universität München, Großhadernerstr. 9, 82152 Planegg-Martinsried, Germany

4 Core Facility Bioimaging and Walter-Brendel-Centre of Experimental Medicine, Biomedical Center, Ludwig-Maximilians-Universität München, Großhaderner Straße 9, 82152, Planegg-Martinsried, Germany

5 Department of Structural Biology, St. Jude Children's Research Hospital, 263 Danny Thomas Place, Memphis, TN, 38105, USA

6 Department of Physiological Chemistry, Biomedical Center, Faculty of Medicine, Ludwig-Maximilians-Universität München, Großhadernerstr. 9, 82152 Planegg-Martinsried, Germany

7 BioPhysics Core Facility, Biomedical Center, Faculty of Medicine, Ludwig-Maximilians-Universität München, Großhadernerstr. 9, 82152 Planegg-Martinsried, Germany

8 Current address: Epigenetics Institute & Department of Cell and Developmental Biology, University of Pennsylvania, Perelman School of Medicine, Philadelphia (PA), USA

24   9 Current address: Department of Clinical Genetics, Rigshospitalet, Copenhagen University

25   Hospital, Blegdamsvej 9, 2100 Copenhagen, Denmark

26   *,# equal contributions

27

28   Correspondence: felix.mueller-planitz@tu-dresden.de, stigler@genzentrum.lmu.de

29 **Summary:**

30 How chromatin enzymes work in condensed chromatin and how they maintain diffusional mobility

31 inside remains unexplored. We investigated these challenges using the *Drosophila* ISWI remodeling

32 ATPase, which slides nucleosomes along DNA. Folding of chromatin fibers did not affect sliding *in vitro*.

33 Catalytic rates were also comparable in- and outside of chromatin condensates. ISWI cross-links and

34 thereby stiffens condensates, except when ATP hydrolysis is possible. Active hydrolysis is also required

35 for ISWI's mobility in condensates. Energy from ATP hydrolysis therefore fuels ISWI's diffusion through

36 chromatin and prevents ISWI from cross-linking chromatin. Molecular dynamics simulations of a

37 'monkey-bar' model in which ISWI grabs onto neighboring nucleosomes, then withdraws from one

38 before rebinding another in an ATP hydrolysis-dependent manner qualitatively agree with our data.

39 We speculate that 'monkey-bar' mechanisms could be shared with other chromatin factors and that

40 changes in chromatin dynamics caused by mutations in remodelers could contribute to pathologies.

41

42

Introduction

43

44   Eukaryotes prevent non-specific, cation-induced aggregation of genomic DNA by wrapping their DNA

45   around histones, thereby forming nucleosomes (Burak et al., 2003; Post & Zimm, 1982). Nucleosomes

46   allow for regulated and reversible condensation of genomic DNA and have evolved as an important

47   medium for epigenetic gene regulation.

48   Nucleosomal DNA can fold into various higher order structures. In low ionic strength environments,

49   chromatin forms an extended structure referred to as the 10-nm fiber (Olins & Olins, 1974; Woodcock,

50   1973). Moderate ionic strength promotes folding into different but defined higher order structures,

51   collectively referred to as '30-nm fibers' (Finch & Klug, 1976). Cellular chromatin, however, appears to

52   assume variable, irregular structures (Ou et al., 2017). It may contain interdigitated 10-nm fibers

53   (Adhireksan et al., 2020; Maeshima et al., 2016) and small folded nodules of chromatin, including tri-

54   and tetranucleosomes (Hsieh et al., 2015; Ricci et al., 2015).

55   Recently, it was discovered that reconstituted chromatin can undergo phase separation (Gibson et al.,

56   2019; Strickfaden et al., 2020). Phase separation is a property of multivalent polymers incl. many

57   proteins and nucleic acids. They can demix from the solution into polymer-rich condensates and a

58   polymer-depleted solution. Biomolecular condensates harbor distinct chemical environments

59   compared to their surrounding solution. They could, for instance, be enriched or depleted for cellular

60   enzymes or metabolites, providing an additional regulatory layer of cellular processes (Y. Zhang et al.,

61   2021).

62   Concentrations can massively increase upon condensate formation. For example, sub-micromolar

63   concentrations of soluble nucleosomes form salt-induced condensates that contain ~0.34 mM

64   nucleosomes (Gibson et al., 2019). Such a high concentration rivals nucleosome concentrations

65   observed in highly condensed metaphase chromosomes *in vivo* (0.52 mM) (Hihara et al., 2012).

66   Most nuclear processes, including transcription and replication, are thought to be inhibited by the

67   presence of nucleosomes (Kornberg & Lorch, 2020). Intuitively, one would expect that folding of

68   chromatin into various higher-order structures and formation of chromatin condensates could pose

69   additional barriers for nuclear factors. For instance, access to specific DNA sequences may be

70   restricted if they are buried deep inside a folded structure, nucleosomal epitopes may become

71   unavailable, enzymes may be excluded from condensates, and even if they are not, diffusion through

72   dense nucleosome fibers may become slow and inefficient. Remarkably, many chromatin enzymes are

73   mobile in the nucleus (Kim et al., 2021). Since the high concentration of nucleosomes in the nucleus

74   well exceeds the dissociation constants (K_D) of most chromatin-associated enzymes, mechanisms must

75   exist that prevent quantitative binding of the enzymes to chromatin and allow sufficient diffusional

76   mobility.

77   We address these and other fundamental questions using *Drosophila melanogaster* ISWI as a

78   prototypical nucleosome remodeling enzyme. ISWI slides nucleosomes along DNA in an ATP

79   hydrolysis-dependent fashion (Längst et al., 1999; Hamiche et al., 1999). It can slide internal

80   nucleosomes in reconstituted nucleosome arrays (Klinker, Mueller-Planitz, et al., 2014; Ludwigsen et

81   al., 2018; Mueller-Planitz et al., 2013; Schram et al., 2015). However, if and how fiber folding and

82   condensation have an impact on nucleosome remodeling has not been systematically investigated,

83   despite the physiological importance (Boyer et al., 2000; Logie et al., 1999). A dense and folded

84   environment could conceivably obstruct remodeling activity, or possibly enhance it as observed for

85   other enzymes (Peeples & Rosen, 2021).

86   **Results**

87   **Intramolecular chromatin folding does not impede remodeling**

88   We reconstituted nucleosomes on DNA with 25 repeats of the Widom '601' nucleosome positioning

89   sequence (Fig. 1a). 13 of these repeats contain a unique restriction site, such as a BamHI site, which

90   becomes exposed during nucleosome remodeling (Ludwigsen et al., 2018; Mueller-Planitz et al.,

91   2013). By measuring accessibility with BamHI, we compared remodeling of folded and unfolded

92   chromatin arrays.

93   After *in vitro* nucleosome reconstitution, three independent quality controls confirmed saturation of

94   array DNA with nucleosomes (Fig. S1a). Analytical ultracentrifugation and negative stain electron

95   microscopy showed intramolecular folding of chromatin arrays but no substantial multimerization at

96   Mg^{2+} concentrations of 1.7 mM. (Fig. 1b, c). A lower Mg^{2+} concentration (0.2 mM) served as a loosely

97   folded control. Whereas single particles exhibited structural heterogeneity in both conditions, their

98   Feret´s diameter decreased, and their circularity increased with increasing Mg^{2+} concentration,

99   consistent with Mg^{2+}-induced intramolecular folding (Fig. 1d, e).

100   Induction of fiber folding by supplementation of Mg^{2+} to 1.7 mM reduced rate constants for

101   remodeling by 2.5±0.2 fold (Fig. 1f, g). Folding however is not the major cause of this drop in activity,

102   as the higher Mg^{2+} concentration also reduced the ATPase activity in presence of non-folding

103   mononucleosomes (Fig. S1b).

104   Internal nucleosomes in nucleosome fibers are more stable and less accessible than external, end-

105   positioned nucleosomes (Hagerman et al., 2009; Poirier et al., 2008, 2009; Schram et al., 2015). To

106   confirm that the effect we observe is not dependent on the linear nucleosome position in an array,

107   we cloned a second version of the 25-mer array, in which the positions of the restriction sites are

108   reversed (Fig. S1c). Supporting our earlier modeling results (Schram et al., 2015), ISWI remodeled

109   nucleosomes with identical rate constants regardless of their location in the array (compare Fig. S1d,

110   e with Fig. 1f, g). We conclude that Mg^{2+}-induced intramolecular folding of the chromatin fiber does

111   not impede nucleosome remodeling by ISWI.

ISWI slides nucleosomes inside chromatin condensates

113   Mg^{2+} also promotes intermolecular interactions between array molecules at elevated array

114   concentrations (Maeshima et al., 2016). Spherical condensates formed upon addition of

115   physiologically relevant concentrations of Mg^{2+} (1 mM and 5 mM Mg^{2+}; Fig. 2a) (Gibson et al., 2019;

116   Strickfaden et al., 2020). The physical nature of these condensates can range from liquid- to solid-like

117   depending on conditions and nucleosome array length (Gibson et al., 2019, 2023; Strickfaden et al.,

118   2020).

119   Given their high nucleosome concentrations, these condensates could potentially exclude large

120   protein complexes. To determine the size exclusion limit of the condensates, we used a series of

121   fluorophore-labeled dextrans of different molecular weights and determined their partition

122   coefficients (Fig. 2b). Dextrans were progressively excluded from chromatin with increasing molecular

123   mass. Nevertheless, even 500 kDa dextrans, which possess a Stokes radius (15.1 nm) (Goins et al.,

124   2008) equivalent to a 6 MDa protein complex, were able to enter the condensates. The data suggest

125   that the chromatin condensates are porous or pliable enough to accommodate large particles.

126   Our dextran results encouraged us to evaluate whether ISWI can also penetrate condensates. We

127   premixed GFP-labeled ISWI with Cy3-labeled chromatin arrays in the absence of nucleotides and

128   induced phase separation by addition of Mg^{2+}. ISWI-GFP was strongly enriched in condensates (Fig.

129   2c). Control experiments proved that GFP or ISWI-GFP did not form condensates by themselves and

130   that GFP on its own does not enrich in chromatin condensates (Fig. 2c and Fig. S2a). Importantly, order

131   of addition experiments showed that ISWI-GFP could penetrate condensates even after their

132   formation with similar efficiency (Fig. 2c). ISWI reached a concentration of ~4 µM in condensates (Fig.

133   S2b).

134   The intermolecular interactions between nucleosomes in condensates could conceivably prevent

135   ISWI-mediated sliding of nucleosomes. Using the restriction enzyme accessibility assay, we clearly

136   detected remodeling under condensate conditions (5 mM Mg^{2+}; Fig. 2d and Fig. S2c). The observed

137   rate constant for sliding was reduced about eight-fold at the higher Mg^{2+} concentration. Condensation,

138   however, is not the major cause of this drop in the activity, as the higher Mg^{2+} concentration also

139   reduced the ATPase activity in presence of mononucleosomes to a similar extent (Fig. S1b).

140   To test if remodeling takes place inside of condensates, we developed an imaging-based nucleosome

141   sliding assay (Fig. 2e). We employed double-fluorophore labeled mononucleosomes that can report

142   on nucleosome sliding via changes in FRET (Yang & Narlikar, 2007). These FRET nucleosomes readily

143   partitioned into condensates (Fig. S2d). FRAP of individual condensates showed little exchange of the

144   FRET nucleosomes between the condensate and the surrounding dilute phase (Fig. S2e). Fluorescence

145   lifetime imaging (FLIM) then allowed us to image FRET levels in- and outside of condensates. The

146   donor lifetime of FRET nucleosomes was quenched compared to nucleosomes that were only labeled

147   with the donor fluorophore or whose acceptor fluorophore was bleached, confirming FRET (Fig. 2f and

148   Fig. S2f, g). Importantly, addition of ISWI and Mg-ATP to FRET nucleosomes, but not to donor-only

149   nucleosomes, increased the donor lifetime, indicative of nucleosome sliding (Fig. 2f and Fig. S2f). Time

150   course measurements after flowing in Mg-ATP to ISWI-containing condensates reveal a steady

151   increase in the fluorescence lifetime (Fig. 2g, Movie S1). No lifetime changes were recordable after

152   addition of the non-hydrolyzable ATP analog Mg-AMPPNP as a negative control (Movie S2). We

153   conclude that FLIM-FRET is a sensitive technology to visualize nucleosome sliding with spatial

154   resolution.

155   To quantify if and to what extent condensates pose a barrier for remodeling, we determined the initial

156   velocities for nucleosome sliding inside condensates (0.77 ± 0.06 s^{-1}) and compared it to remodeling in

157   solution (2.15 ± 0.15 s^{-1}). We obtained the latter by using mononucleosomes that do not phase separate

158   under these conditions at equivalent bulk concentrations (1.2 µM) under otherwise identical

159   conditions (Fig. 2h). Use of five times higher Mg-ATP concentrations gave similar results (Fig. S2h),

160   arguing that Mg-ATP was saturating both in solution and condensates. ISWI concentrations inside

161   condensates were substoichiometric, reaching 4.7 ± 0.6 µM (Fig. S2b), which is well below the

162   nucleosome concentration in condensates (225 ± 59 µM; see below). In summary, condensates slowed

163   down remodeling by 2.6-fold, suggesting that condensation poses no substantial barrier for

164   remodeling; instead it may fine tune the remodeling activity.

165   **ISWI requires active hydrolysis to diffuse through condensates**

166   Nucleosome concentrations inside of condensates reach remarkably high levels, 225 ± 59 µM,

167   equivalent to ~45 g/l, as determined by holotomography (Fig. 3a), a label-free methodology that can

168   determine concentrations from the refractive index. Our measurement using 25-mer arrays agreed

169   well with previous estimates that employed 4- and 12-mer nucleosome arrays (195 to 550 µM) using

170   electron tomography and fluorescence microscopy (Gibson et al., 2019; M. Zhang et al., 2022). A broad

171   range of conditions (array length and buffer conditions) thus leads to relatively static nucleosome

172   densities in condensates. Of note, *in vivo* nucleosome concentrations fall into the same regime (100

173   µM to 500 µM) (Hihara et al., 2012; Weidemann et al., 2003), making *in vitro* condensates a model for

174   studying challenges encountered by chromatin enzymes in the crowded nucleus.

175   At such a high concentration, well above the dissociation constant of ISWI (<1 µM; (Leonard & Narlikar,

176   2015)), the enzyme would be expected to be constantly bound to nucleosomes, presumably limiting

177   its mobility. Yet, we found above that condensates do not abrogate remodeling, suggesting a certain

178   mobility of the enzyme.

179   To probe ISWI´s dynamics inside condensates, we performed FRAP of GFP-labeled ISWI. After

180   bleaching the central area of condensates, there was a poor recovery in the absence of nucleotides

181   and with saturating concentrations of Mg-ADP or Mg-AMPPNP (Fig. 3b and Fig. S3a), consistent with

182   the expectation that ISWI is highly immobile in condensates. Strikingly, however, Mg-ATP addition

183   rendered ISWI strongly dynamic, suggesting that active ATP hydrolysis is required not only for

184   productive remodeling, but also to ensure rapid diffusion of ISWI within condensates.

185   **ATP hydrolysis prevents ISWI-mediated hardening of condensates**

186   An intriguing model to explain the mobility of ISWI through condensates in the presence of ATP would

187   be that chromatin remodeling by ISWI makes the condensate more fluid. ISWI would essentially act

188   as a 'molecular stir bar' (Larson & Narlikar, 2018). However, fluorophore-labeled nucleosome arrays

189   were not mobile, as assessed by FRAP, even after prolonged incubation with ISWI and Mg-ATP (Fig.

190   S3b). We conclude that enhanced fluidity of chromatin upon remodeling is unlikely to explain efficient

191   diffusion of ISWI in presence of ATP.

192   ISWI has two known DNA binding domains, its ATPase domain and its HSS domain (Grüne et al., 2003),

193   allowing it to bind two nucleosomes (Bhardwaj et al., 2020; L. Li et al., 2023; Yamada et al., 2011)

194   potentially on neighboring DNA fibers. ISWI-mediated bridges between neighboring fibers would alter

195   mechanical properties of condensates. To test this prediction, we employed optical tweezers to fuse

196   condensates in a controlled manner (Fig. 3c) and recorded the fusion velocity (Fig. S3c), which depends

197   on the viscoelastic properties of condensates (Wang et al., 2018). The number of fusion events

198   decreased with the length of the nucleosome array, consistent with a recent report (Muzzopappa et

199   al., 2021), and with increased Mg^{2+} concentration (Fig. S3d). Higher ISWI concentrations also slowed

200   down the fusion velocity (Fig. S3e), which, at least partially, can be explained by an increase in viscosity

201   (Fig. S3f). For these reasons, the following experiments were performed with 13mer arrays in 1 mM

202     $MgCl_2$ and substoichiometric ISWI amounts, typically 1:5 ISWI to nucleosomes.

203   Compared to nucleotide-free ISWI, the fusion velocities drastically slowed down when we added Mg-

204   AMPPNP, Mg-ADP-BeF_x or Mg-ADP to ISWI-containing condensates (Fig. 3d, Movie S3). The presence

205   of ISWI's HSS domain was required for this effect (Fig. 3e). Fusion velocities also shrank when we

206   added Mg-ATP to an ATP hydrolysis-defective ISWI mutant ($ISWI_{E257Q}$; Fig. 3f). Strikingly, however, Mg-

207   ATP did not slow down fusion when we used wild-type ISWI instead (Fig. 3g, Movie S4). In control

208   experiments, we ruled out that nucleotides or excess Mg^{2+} that is added together with nucleotides

209   caused strong effects on fusion independent of ISWI (Fig. S3g).

210   We conclude that ISWI, when stuck in individual nucleotide states, stiffens condensates. The HSS

211   domain participates in this process, likely by forming bridges to a neighboring nucleosome. It is active

212   hydrolysis, in other words the active cycling through all nucleotide states, that prevents ISWI from

213   stably bridging nucleosomes.

214   **A theoretical framework to describe ISWI diffusion in condensed chromatin**

215   We next derived a model for ISWI-chromatin interactions in condensates. The two DNA binding

216   domains of ISWI, the ATPase and the HSS domain, are flexibly linked (Ludwigsen et al., 2013) and

217   undergo large conformational changes during the ATPase cycle (Harrer et al., 2018; Leonard &

218   Narlikar, 2015). These conformational changes might allow ISWI to make and break interactions with

219   neighboring nucleosomes during the ATPase cycle.

220   When ISWI binds two nucleosomes on different DNA fibers at once, nucleosome condensates should

221   stiffen, leading to slower condensate fusion. The drastically slower fusion velocities that we observed

222   when ISWI was bound to ADP, AMPPNP or ADP-BeF_x therefore indicate that ISWI can bridge

223   nucleosomes in these nucleotide states (Fig. 3d, e). Of note, bridge formation is nucleotide-state

224   dependent. Addition of nucleotide-free ISWI to condensates had only a modest impact on fusion

225   velocity, suggesting that nucleotide-free ISWI only forms unstable bridges. Yet, it is still stably bound

226   to chromatin as suggested by FRAP (Fig. S3a). Taken together, the results indicate that only one of

227   ISWI's domains interacts with chromatin in the nucleotide-free state.

228   ISWI FRAPs slowly in its AMPPNP, ADP-BeF$_x$ and ADP-bound states, suggesting that ISWI interacts with

229   nucleosomes with at least one of its binding domains in all these states. Intriguingly, ISWI FRAPs

230   rapidly in the presence of ATP. It is thus the progression through ISWI's ATPase cycle that repeatedly

231   modulates the binding affinities of both binding domains. Hydrolysis-powered conformational

232   changes would also repeatedly break up nucleosome-nucleosome bridges, explaining why addition of

233   ATP prevents stiffening of condensates in condensate fusion experiments. We refer to this model as

234   a "monkey bar" mechanism (Rudolph et al., 2018) as it results in an alternating release of one or the

235   other binding site during the ATPase cycle (Fig. 4a).

236   ADP-bound and nucleotide-free ISWI display different behavior in fusion and FRAP experiments. ISWI

237   in both states FRAPs slowly, whereas ISWI in the ADP but not the nucleotide-free state stiffens

238   condensates. This difference suggests that the two interaction sites have individual nucleotide state-

239   dependent binding affinities for nucleosomes. In both ADP-bound and nucleotide-free ISWI, one

240   domain has a higher binding affinity than the other. The FRAP rate will be dominated by the higher

241   affinity interaction. The fusion speed, on the other hand, also relies on the strength of the weaker

242   affinity of the other domain. In the ADP-bound state, the weaker interaction domain therefore likely

243   possesses an affinity that is higher than in the nucleotide-free state.

244   We formalized these findings in terms of a simple kinetic model (Fig. S4a). In the ATP state, ISWI stably

245   binds with both domains to two nucleosomes. Upon hydrolysis, a conformational change weakens

246   one of the interactions and leads to the release of one nucleosome. Subsequent ADP release switches

247   the strengths of the two interactions, leading to rebinding of the first domain to a nucleosome, while

248   releasing the second nucleosome. This alternating binding and unbinding of the two domains would

249   enable ISWI to actively move through a dense mesh of nucleosomes and prevent ISWI from stably

250   crosslinking neighboring fibers.

251   To test if such a simple, idealized model could recapitulate our observation that ATP hydrolysis allows

252   fast FRAP and prevents condensate hardening in fusion experiments, we performed molecular

253   dynamics simulations using Rouse chains to model chromatin arrays and describing all other

254   interactions using Lennard-Jones potentials (Fig. S4b-d). Different nucleotide states of the remodeler

255   were modeled by changing the depth of the respective interaction potentials.

256   In ISWI FRAP simulations (Fig. 4b, Movie S5), we observed enhanced recovery of the remodeler in the

257   case of active ATP hydrolysis compared to remodeler that was stalled in any other nucleotide state

258   (Fig. 4c). Like experiments, simulations of fusion (Fig. 4d, Movie S6) show no significant difference

259   between ATP and nucleotide free conditions (Fig. 4e). The ADP and AMPPNP conditions are noticeably

260   slower and do not reach full circularity within the simulated time. This again hints at the formation of

261   ISWI-mediated stably bridged chromatin networks in the condensates that leads to a decrease in

262   condensate fluidity.

263   **Discussion**

264   One major result of our study is that the nucleosome remodeling enzyme ISWI can work largely

265   unimpeded in folded and condensed nucleosome environments. This conclusion likely extends to

266   other remodeling complexes given that their remodeling activities were minimally affected by histone

267   hyperacetylation or trypsinization (Boyer et al., 2000; Logie et al., 1999). Our finding implies that all

268   nucleosomes are similarly accessible for the enzyme in condensed arrays. As nucleosome sliding takes

269   place in 1 bp increments (Deindl et al., 2013), each bp movement induces a rotation of the nucleosome

270   by ~36° relative to other nucleosomes. Sliding inside condensed arrays, therefore, necessitates that

271   the chromatin structure is highly fluid and readily accommodates large, local structural changes

272   imposed by nucleosome sliding.

273   ISWI critically depends on interactions to the H4 N-terminal tail and the nucleosome acidic patch for

274   catalysis (Clapier et al., 2001; Dann et al., 2017; Gamarra et al., 2018). Incidentally, both these epitopes

275   are also suggested to be important for array folding (Schalch et al., 2005). The fact that catalysis is not

276   strongly impaired in condensed nucleosomes suggests that these epitopes are still dynamically

277   available for ISWI.

278   Nucleosome concentrations in condensates reach ~0.2 mM, a regime that nuclear enzymes also

279   encounter *in vivo* (Hihara et al., 2012; Weidemann et al., 2003). We show that despite this high

280   concentration, condensates remain viscoelastic materials and can accommodate dextrans with a

281   Stokes radius equivalent to a 6 MDa protein complexes. Thus, even large remodeling complexes and

282   other nuclear machines retain a chance to enter condensed chromatin, consistent with prior literature

283   (Beaudouin et al., 2006; Erdel et al., 2015; Verschure et al., 2003; M. Zhang et al., 2022).

284   ISWI strongly enriches in chromatin condensates, further illustrating condensate plasticity. We

285   anticipate that the same will be true for other chromatin factors simply because they possess high

286   affinities for nucleosomes. It is as if chromatin is the scaffold in condensates to which client proteins

287   like ISWI bind. This simple scaffold-client concept, often entertained in condensate biology (Ditlev et

288   al., 2018), does not capture the complexity of the reaction, however. Inevitably, the client will affect

289   chemical and physical properties of the scaffold. We found, for instance, that binding of ISWI hardens

290   chromatin condensates, probably by crosslinking fibers. Remodelers, therefore, could serve structural

291   purposes in addition to their well-known enzymatic activities (Korber & Becker, 2010).

292   The biophysical properties of nucleosome condensates varied with ambient conditions. Increasing

293   Mg^{2+} concentrations, for instance, drastically stiffened condensates. As free Mg^{2+} increases during

294   mitosis (Maeshima et al., 2018), stiffening of chromatin could facilitate sister chromatid condensation

295   (Shimamoto *et al.*, 2017). Moreover, changes in the extracellular milieu could rapidly elicit cellular

296   responses through changes in viscoelastic properties of cellular components, including chromatin

297   (Kroschwald et al., 2018; Munder et al., 2016).

298   Biomolecular condensates are suggested to affect enzyme activities through their unique chemical

299   environments (Zhang et al., 2021). Performing enzyme kinetics in non-homogeneous solution is a

300   challenge. Here, we have developed a FLIM-FRET nucleosome sliding assay to overcome such

301   limitations. Its spatial resolution allows us to compare nucleosome sliding in- and outside of

302   condensates. We predict that this kind of technology could become beneficial in the future for tracking

303   enzymatic processes in cellular condensates in real time.

304   Enzymatic reactions inside biological condensates were suggested to benefit from high concentration

305   of components (Zhang et al., 2021). However, rate enhancements would be expected for enzymes

306   that have to work at subsaturating substrate concentrations. This is not the case for remodelers, which

307   face nucleosome concentrations in the nucleus far above their K_D, explaining why ISWI did not

308   experience rate enhancements upon condensate formation.

309   Regardless of the mode and extent of chromatin phase separation occurring *in vivo* (Erdel et al., 2020;

310   Erdel & Rippe, 2018; Keizer et al., 2022; Schneider et al., 2022), we view nucleosome condensates as

311   useful model systems to study challenges enzymes face at the enormously high nucleosome

312   concentrations in the nucleus. For instance, multivalent recognition of the nucleosome paired with

313   the high nucleosome concentration could promote non-productive interactions (Mueller-Planitz et al.,

314   2013). Given that nucleosome concentrations generally far exceed K_D-values of chromatin enzymes,

315   almost all enzyme molecules would be expected to be bound to chromatin at equilibrium. Our FRAP

316   data support that notion, showing that ISWI becomes stuck in condensates if ATP cannot be turned

317   over. This finding also helps explain why ATPase-dead variants of ISWI are easier to ChIP (Gelbart et

318   al., 2005; Whitehouse et al., 2007) even though nucleotides only weakly modulate affinities (Leonard

319   & Narlikar, 2015). How, then can these enzymes be mobile enough to rapidly diffuse through

320   chromatin? ISWI could mobilize ("stir up") chromatin by shuffling nucleosomes around, but we found

321   no evidence in support of this possibility.

322   Instead, we propose the existence of a novel functionality of ISWI's ATPase activity: besides

323   nucleosome sliding, ATP hydrolysis may power conformational changes that pull the nucleosome

324   binding domains of ISWI away from nucleosomes, leading to dissociation and subsequent re-

325   association to other nucleosomes. Non-productive interactions could be dissolved in this fashion, and

326   we speculate that some of the frequent pauses that ISWI remodelers take during sliding could be

327   caused by unproductive binding (Blosser et al., 2009; Deindl et al., 2013). According to this mechanism,

328   ISWI effectively remains bound to nucleosomes at any time, yet active ATP hydrolysis fuels its diffusion

329   through chromatin. At the same time, hydrolysis prevents ISWI from crosslinking and thereby

330   hardening condensates. This mechanism may be shared with other fly and yeast remodelers, which

331   also became more dynamic in presence of ATP (Kim et al., 2021; Tilly et al., 2021). The mechanism

332   however may not extend to Snf2H and Snf2L transfected into human cells, which were mobile before

333   and after ATP depletion (Erdel et al., 2010). These remodelers may rely on a different mechanism,

334   perhaps due to heteromerization (Oppikofer et al., 2017).

335   Our findings add another facet to why loss of function mutations can induce dominant negative

336   phenotypes or be cancer-associated (Clapier et al., 2020). Half of SMARCA4 mutations in cancers lie in

337   the ATP cleft and these mutants show slower FRAP (Hodges et al., 2018). Expression of ATPase dead

338   BRM in *Drosophila* caused peripheral nervous system defects, homeotic transformations, and

16

339 decreased viability (Elfring et al., 1998). All phenotypes were dominant negative (Elfring et al., 1998;

340 Hodges et al., 2018) and might be caused in part by changes in chromatin dynamics, and not

341 exclusively by disruption of canonical remodeler functions. Changed dynamics of biomolecular

342 condensates may in turn disturb biological functions (Li et al., 2020; Shi et al., 2021). It is our hope that

343 our tools and concepts will help open new avenues for mechanistic dissections and development of

344 therapeutics.

345 **Methods**

346 **Cloning**

347 *Cloning of GST-sfGFP and 6xHis-TEV-ISWI-3C-STREP-sfGFP*

348 Full length super fold GFP (Pédelacq et al., 2006) sequence was amplified from the plasmid generously

349 provided from Ökten group at TU Munich (pFMP248). The PCR product and pET41b(+) were digested

350 with *BglII* and *EcoRI*, ligated and the resulting plasmid containing GST-sfGFP construct (pFMP241)

351 amplified in *E. coli DH5α*. Correct sequence was confirmed by Sanger sequencing.

352 To make 6xHis-TEV-ISWI-3C-STREP-sfGFP construct, the PCR amplified sfGFP sequence was first

353 subcloned into vector pUC57 containing synthesized (GenScript) C-terminus for 3C-STREP-KKCKK-

354 GFP11 (pFMP249). For that purpose, both insert and vector were digested with *MslI* and *HindIII*. *MslI*

355 cuts inside of GFP11 (extreme C-terminal sequence of sfGFP) and leaves six residues. The obtained

356 plasmid was then digested with *XbaI* and *HindIII* and ligated into pFMP210 digested with the same

357 enzymes, and pFMP244 was produced and amplified in *E. coli DH5α*. Correct sequence was confirmed

358 by Sanger sequencing.

359 **Protein expression and purification**

360 *GFP expression and purification*

361   Plasmid containing GST-GFP (pFMP248) was transformed into *E.coli* BL21 (DE3) and incubated on

362   selective plate at 37 °C overnight. A single colony was inoculated into 15 mL LB media supplemented

363   with ampicillin and grown overnight at 37 °C. The next morning the culture was diluted to OD=0.05,

364   grown at 37 °C until OD=0.6 and induced with 0.2 mM IPTG. Protein was expressed overnight at 20 °C

365   with shaking. The bacterial cultures were harvested (rotor SS34, 14000 rpm, 10 min) and pellet was

366   stored at -80 °C. Pellet from 485 mL expression was resuspended in 20 mL of GST binding buffer (25

367   mM Tris-HCl pH=7.5, 150 mM NaCl, 1 mM EDTA, 0.5 mM DTT, 20 mM imidazole, 1 mM PMSF, 30 μL

368   of each leupeptin, pepstatin, aprotinin and one tablet complete EDTA-free protease inhibitor cocktail

369   (Roche)). Cells were disrupted in French press (3x 1500 PSI) and sonication (12x10 s on, 20 s off,

370   amplitude 22%). The suspension was centrifuged (SS34 rotor, 19000 rpm, 30 min, 4 °C) and to the

371   supernatant 1 mL of prewashed GST-beads was added (50% slurry). The suspension was incubated for

372   90 min at 4 °C with gentle mixing. The beads were removed with centrifugation (1000 rpm, 1 min, 4

373   °C) and washed five times with 10 mL binding buffer. Finally, beads were resuspended in 1.5 mL elution

374   buffer (50 mM Tris-HCl pH=8.0, 10 mM reduced glutathione, 5% glycerol) and incubated on rotating

375   wheel for 30 min at 4 °C. The beads were removed by centrifugation and supernatant aliquoted, frozen

376   in liquid nitrogen and stored at -80 °C.

377   *Expression and purification of ISWI, ISWI-GFP, ISWI$_{\Delta HSS}$ and ISWI E257Q*

378   Corresponding plasmids containing *D. melanogaster* ISWI (pFMP210 for 6xHis-TEV-ISWI, pFMP244 for

379   6xHis-TEV-ISWI-3C-STREP- sfGFP, pFMP114 for 6xHis-TEV-ISWI26−648 (*ISWI$_{\Delta HSS}$*), pFMP110 for 6xHis-

380   TEV-ISWI E257Q) were freshly transformed into BL21 Star *E. coli* and plates were incubated at 37 °C

381   overnight. The bacterial lawn from one plate was harvested and used to inoculate two l of LB media.

382   Cultures were grown (37 °C, 130 rpm) until OD 0.5-0.6 when they were induced with 1 mM IPTG. The

383   expression went overnight at 18 °C with shaking. The bacterial cultures were harvested (6000xg, 10

384   min, 4 °C). Pellets were gently rinsed with cold water and stored at -80 °C. Except for ISWI$_{\Delta HSS}$, whose

385   purification is described in previous publications (Harrer et al., 2018; Mueller-Planitz et al., 2013), all

386   ISWI proteins were purified as follows. Cells were thawed in a palm of a hand with occasional vortexing

387   and resuspended in HisA buffer (50 mM Tris-HCl pH=7,4, 300 mM NaCl, 0.5 mM DTT) supplemented

388   with 20 mM imidazole (pH=7.4), 1 tablet complete-EDTA free protease inhibitors (Roche), as well as

389   leupeptin (1 mg/L), pepstatin (0.7 mg/L) and aprotinin (1 mg/L). Benzonase (Merck Millipore

390   1016540001 100000; 5 µl per liter of culture) and lysozyme (tip of a spatula) were added and

391   suspension was sonicated on ice (Branson sonifier, 6x10 seconds on, 10 seconds off, amplitude 25%).

392   The homogenized bacteria were then cracked with six runs on Microfluidizer LM10 at 1200 bar.

393   Lysates were centrifuged (19000 rpm, JA25.50 rotor, 4 °C, 30 min), supernatants filtered through 0.45

394   µm syringe filter and loaded onto His Trap (5 mL, GE Healthcare) equilibrated with 5% HisB buffer

395   (100% HisB; 50 mM Tris-HCl pH=7,4, 300 mM NaCl, 400 mM imidazole). The column was washed with

396   10 column volumes (CV) 5% HisB, then with 6 CV 10% HisB and 1 CV 20% HisB. ISWI was then eluted

397   with 20-100% HisB gradient over 10 CV. ISWI containing fractions were pooled, TEV protease added

398   (0.1 mg for every 8 mg of ISWI) and the mixture was dialyzed (Spectra/Por dialysis membrane, cutoff

399   12000-14000 kDa) overnight against dialysis buffer (15 mM Tris-HCl pH = 7.4, 150 mM NaCl, 1 mM

400   DTT). To remove His-tagged TEV protease, cleaved-off 6xHis-tag and uncleaved 6xHis-TEV-ISWI, a

401   second nickel-affinity chromatography was performed (His Trap, 5 mL, GE Healthcare; equilibrated in

402   10% HisB buffer). Sample was loaded and unbound protein further washed out with 10% HisB. The

403   flowthrough was pooled and its conductivity reduced by slow dilution with two volumes of 2% MonoS

404   B buffer (100% MonoS B =15 mM Tris-HCl pH=7.4, 2 M NaCl, 1 mM DTT), which was diluted with

405   MonoS A (15 mM Tris-HCl, 1 mM DTT) and filtered through 0.2 µm syringe filter. A MonoS column

406   (5/50 GL GE Healthcare 1 mL) was equilibrated with 2% MonoS B. After loading, the protein was eluted

407   with 2-30% MonoS B (10 CV) and 30-100% MonoS B (4 CV). Fractions containing ISWI were pooled

408   together, concentrated and loaded onto the HiLoad Superdex200 (GE Healthcare, 120 mL) exclusion

409   column equilibrated with GF buffer (50 mM Hepes KOH pH=7,6, 0.2 mM EDTA pH=8, 200 mM KOAc,

410   10 mM DTT). ISWI-containing fractions were pooled and protein was concentrated to ~5 mg/mL.

411   Molar concentration was determined by using calculated extinction coefficient (Expasy Protparam

412   tool). Proteins were aliquoted, frozen in liquid nitrogen and stored at -80 °C.

413   *Expression and purification of histones*

414   Codon optimized *D. melanogaster* histones were expressed and purified as previously described

415   (Klinker, Haas, et al., 2014). Corresponding plasmids (pFMP128 for H2A, pFMP129 for H2B, pFMP186

416   for H3, pFMP187 for H4, pFMP269 for H2AK119C, pFMP270 for H3C111A, pFMP268 for H4T1C) were

417   freshly transformed into BL21 Star *E. coli* and incubated at 37 °C overnight. Bacterial lawns from one

418   plate were then used to inoculate two liters of LB media. Cultures were grown (37 °C, 130 rpm) until

419   OD reached 0.5-0.6 when they were induced with 1 mM IPTG. The expression went for three hours at

420   37 °C with shaking. The bacterial cultures were spun down (6000xg, 10 min, 4 °C). Pellets were gently

421   resuspended with cold water, transferred to a 15 ml Falcon tube. Samples were centrifuged and the

422   pellets stored at -80 °C. Cells were thawed in a palm of a hand with occasional vortexing and

423   resuspended in SA buffer (40 mM NaOAc pH=5.2, 1 mM EDTA pH=8, 10 mM lysine) supplemented

424   with 6 M urea, 200 mM NaCl, 1 mg/mL aprotinin, 1 mg/mL leupeptin, 1 mg/mL pepstatin, 1 mM PMSF

425   and 5 mM β-mercaptoethanol. Benzonase (Merck Millipore 1016540001 100000; 5 µl per liter of

426   culture) and lysozyme (tip of a spatula) were added and suspension was sonicated on ice (Branson

427   sonifier, 15 seconds on, 30 seconds off, amplitude 30%, effective sonication time 20 minutes). The

428   homogenized bacteria were then cracked with six runs on Microfluidizer LM10 with 1200 bar. Lysates

429   were centrifuged (19000 rpm, JA25.50 rotor, 4 °C, 30 min), supernatant filtered through 0.45 µm

430   syringe filter and loaded onto a HiTrap Q HP column (5 ml, GE Healthcare) that was stacked on top of

431   a SP column (5 ml, GE Healthcare) equilibrated with 20% buffer B (buffer A: 40 mM NaOAc pH=5.2, 1

432   mM EDTA pH=8, 10 mM lysine, 7.5 M urea, 5 mM DTT; buffer B: 40 mM NaOAc pH=5.2, 1 mM EDTA

433   pH=8, 10 mM lysine, 7.5 M urea, 5 mM DTT, 1000 mM NaCl). Samples were applied to the stacked

434   columns. The columns were washed with 20% buffer B (1 CV). The Q column was removed and SP

435   column further washed with 25% buffer B (3 CV) and 30% buffer B (3 CV). Histone was eluted with 30-

436   40% buffer B gradient (5 CV), 40-80% buffer B gradient (7 CV), 100% buffer B (3 CV). Pooled fractions

437   were dialyzed (SpectraPor MWCO 3,500 kDa) three times against 5 L of miliQ water. Purity was

438   analyzed on SDS-PAGE and concentration determined from A280 absorption. Histones were aliquoted

439   (1 mg per aliquot), flash frozen in liquid nitrogen and stored at -80 °C or -70 °C. Histones were

440   lyophilized before use. Lyophilized histones were stored at -20 °C.

441   *Assembly and purification of octamers*

442   Lyophilized histone aliquots were dissolved in an unfolding buffer (20 mM Tris-HCl, 7 mM

443   guanidinium-HCl, 20 mM DTT) to 4 mg/ml for 10 minutes in a thermoblock (24 °C, 600 rpm). Solutions

444   were spun down in table top centrifuge (10 minutes, full speed, 4 °C), and supernatants transferred

445   to fresh tubes and kept on ice until dialysis. Histone concentrations were remeasured in unfolding

446   buffer by measuring OD280 and corrected for purity as assessed from SDS-PAGE gel. Histones were

447   mixed in molar ratio H2A:H2B:H3:H4=1.4:1.4:1:1. The histone mixture was transferred into dialysis

448   membranes (Roth E658.1 MWCO: 4000-6000) which were soaked in water for one hour and rinsed

449   with refolding buffer (10 mM Tris-HCl pH=7.5, 2 M NaCl, 1 mM EDTA, 5 mM β-mercaptoethanol). The

450   mixture was then dialyzed three times against 1 L of refolding buffer, with the second dialysis step

451   being overnight. Lastly, octamers were purified by size exclusion chromatography (HiLoad 16/60

452   Superdex 200 prep grade), concentrated to 4 mg/mL (Amicon 15 mL 30 kDa), aliquoted, flash frozen

453   in liquid nitrogen and stored at -80 °C or -70 °C.

454   *Histone labeling (H2AK119C-atto565, H4T1C-cy3)*

455   Lyophilized histone aliquots were dissolved in a labeling buffer (7 M guanidinium-HCl, 20 mM Tris-HCl

456   pH=7.5, 5 mM EDTA, 0.7 mM TCEP) to final concentration 0.2 mM and incubated two hours to reduce

457   all cysteines. Cyanin-3-maleimide (Lumiprobe) was dissolved in DMSO to final concentration 100 mM

458   and added to solution in 5.7 fold excess. Atto-565 maleimide (Atto-tec) was dissolved in DMF to final

459   concentration 100 mM and added to solution in 13.2 fold excess. Histones were incubated with the

460   dye for 14 hours (3 hours for cy3 labeling) on rotating wheel at room temperature covered with

461   aluminum folium. To stop the labeling reaction, β-mercaptoethanol was added to final concentration

462   to 340 mM. For cy3 labeling, reaction was stopped by adding DTT to final concentration 20 mM.

463   Unreacted dye was partially removed by several rounds of ultrafiltration (15 mL 10K Amicon,

464   Millipore) and successive dilutions with labeling buffer (this step was omitted for Cy3 labeling). The

465   labeling efficiency was assessed with SDS-PAGE and fluorescence imaging.

466   **Synthesis of DNA for nucleosome arrays**

467   To distinguish remodeling of individual nucleosomes in a nucleosome array, we previously cloned a

468   DNA with unique restriction sites in 13 of 25 Widom-601 positioning sequences with a 197 bp repeat

469   length (pFMP233) (Ludwigsen et al., 2018) (Fig. S1c). Here we cloned a second variant of this DNA by

470   placing the 13 unique restriction sites on the other end of the canonical 601 sites, essentially inverting

471   the unique restriction sites with regards to their positioning inside of the array, yielding pFMP232 (Fig.

472   1a). To this end, thirteen 601 repeats were synthesized (GenScript) in which naturally occurring AvaI

473   and AluI sites in the canonical 601 sequenced were replaced with unique restriction sites. A unique

474   AvaI restriction site was added to the 3´-end (pFMP226). The 13-mer was extended to a 25-mer as

475   follows. pFMP226 was completely digested with XbaI, EcoRI and AseI in buffer II (NEB) and the insert

476   was subcloned into pUC18, which was fully digested with XbaI and EcoRI, yielding pFMP236. A plasmid

477   containing 25x197 bp canonical Widom-601 repeats (pFMP166) was subjected to partial AvaI

22

478   digestion. The band corresponding to a 12mer repeat (2354 bp) was gel purified and cloned via ligation

479   into AvaI digested pFMP236, yielding pFMP232 (Fig. 1a).

Preparation of DNA for nucleosome arrays

481   25mer and 13mer nucleosome arrays were prepared as published previously (Ludwigsen et al., 2018).

482   Briefly, plasmids carrying 25 (pFMP232, pFMP233) or 13 (pFMP226) consecutive copies of 197 bp with

483   modified 601 sequence were transformed into DH5α *Escherichia coli* strain and purified from four

484   liters of culture by using plasmid DNA purification kit Nucleobond® PC 10000 (Macherey-Nagel). Three

485   mg of the plasmids were digested with EcoRI HF (0.25 U/µg DNA) and HincII (0.6 U/µg DNA) in

486   CutSmart Buffer at 37°C for 3 h to cut out the arrays from the plasmids. When the digest was complete,

487   restriction enzymes were heat-inactivated by incubation at 65°C for 20 min. Tubes were put on ice

488   before AseI was added (0.5 U/ µg DNA) and then incubated at 37 °C for four h. After digest was

489   complete, DNA was purified via phenol/chloroform extraction and ethanol precipitated in presence of

490   NaOAc. Finally, it was resuspended in TE buffer (10 mM Tris-HCl pH=8, 1 mM EDTA pH=8) and stored

491   at -20 °C.

Preparation of DNA for mononucleosomes

493   DNA fragments containing the 601 sequences were amplified by large-scale PCR (Yang & Narlikar,

494   2007). Primers were obtained from Sigma. For primer sequences, see Table S1. The PCR was cleaned

495   up by precipitating the plasmid template by addition of ½ of volume 30% PEG 8000 (w/w) in 30 mM

496    $MgCl_2$. The PCR product was then precipitated by adding the same volume of propan-2-ol. The pellet

497   was washed with 70% (v/v) cold ethanol, resuspended in TE buffer and stored at -20 °C.

Chromatin assembly and purification

499   *Assembly of 25- and 13mer arrays*

23

500 The optimal molar octamer:601 ratio was identified by performing small scale test assemblies, where

501 purified octamers were titrated to 7.5 µg digested plasmid (Ludwigsen et al., 2018). Preparative

502 assembly contained 100-500 µg digested plasmid (100 ng/µL of 601-array DNA, which corresponds to

503 150 or 200 ng/µL of total digested plasmid containing 25mer or 13mer, respectively). It also contained

504 corresponding amounts of purified octamers, 2 M NaCl, 10 mM Tris-HCl pH=7.6, 1 mM EDTA pH=8, 1

505 mM DTT. Reactions were transferred into dialysis membrane and underwent salt gradient dialysis: 3

506 L of low salt buffer (50 mM NaCl, 10 mM Tris-HCl pH=7.6, 1 mM EDTA pH=8, 1 mM DTT) was pumped

507 into 1 L of high salt buffer (2 M NaCl, 10 mM Tris-HCl pH=7.6, 1 mM EDTA pH=8, 1 mM DTT) containing

508 the dialysis bag over a period of 24 hours. To maintain the constant volume, buffer was simultaneously

509 pumped out with the same speed. Assemblies were then dialyzed against 1 L of low salt buffer before

510 they were precipitated by addition of equal volume of precipitation buffer (10 mM Tris–HCl pH 7.6, 7

511 mM or 10 mM $MgCl_2$ for 25mer or 13mer, respectively). Pellets were resuspended in TE buffer (10

512 mM Tris-HCl pH=7.6, 1 mM EDTA pH=8) and quality controls of chromatin array were performed as

513 described (Ludwigsen et al., 2018) (Fig. S1a). Chromatin concentrations were approximated by UV

514 assuming that 1 OD at 260 nm equals 50 ng/µL of DNA.

515 *Mononucleosomes*

516 The optimal molar octamer:DNA ratio was first identified by titrating octamers to DNA. Preparative

517 assemblies contained DNA (200 ng/µL), purified octamers, 2 M KCl, 20 mM Tris-HCl pH=7.7, 10 mM

518 DTT. Reactions were transferred into Slide-A-lyzer 7k Mini and underwent salt gradient dialysis in 200

519 mL of Mono2000 buffer (2 M KCl, 20 mM Tris-HCl pH=7.7, 0.1 mM EDTA pH=8, 1 mM DTT) to which 1

520 L of Mono0 buffer was pumped (20 mM Tris-HCl pH=7.7, 0.1 mM EDTA pH=8, 1 mM DTT) over 24

521 hours. To maintain constant volume, buffer was simultaneously pumped out with the same speed.

522 Assemblies were dialysed against Mono0 buffer and purified over 10-30% (w/w) glycerol gradient.

523 Concentrations were determined as above for arrays.

524 **Quality controls of assembled chromatin**

525 *Agarose gel of nucleosome arrays*

526 200 ng of before and after Mg-precipitation was analyzed by agarose gel electrophoresis (0.7%).

527 *NotI digestion of nucleosome array*

528 200 ng of arrays were digested in EX50 buffer (10 mM Hepes–KOH pH 7.6, 50 mM KCl, 1.5 mM $MgCl_2$,

529 0.5 mM EGTA) with Not1 (20 U/μL) in total volume of 15 μL for three hours at 26 °C. Digestion was

530 analyzed on 1.1% agarose.

531 *BsiWI digestion of nucleosome array*

532 250 ng of an arrays were digested in buffer (25 mM Hepes–KOH pH 7.6, 0.1 mM EDTA, 50 mM NaCl,

533 10% glycerol, 2 mM $MgCl_2$) with BsiWI (10 U/μL) for 1 hour at 26 °C in total volume of 20 μL. The

534 digestion was stopped with addition of SDS (final concentration 0.4%) and EDTA (final concentration

535 20 mM) followed by Proteinase K (1 mg/mL) treatment in total volume of 30 μL for three hours at 65

536 °C or overnight at 37 °C. DNA was ethanol precipitated and analyzed on 1% gel.

537 **Analytical ultracentrifugation**

538 Sedimentation velocity (SV) experiments of purified, reconstituted arrays were conducted at 20 °C in

539 a Beckman Coulter Optima XL-I analytical ultracentrifuge (Palo Alto, CA) using an An-50 Ti rotor.

540 Samples contained 21.6 ng/μL (6.9 nM) of 25mer and were dissolved in buffer (1 mM Tris-HCl pH 8.0,

541 0.01 mM EDTA pH 8.0, 0.01 mM DTT, 50 mM NaCl, 0.2 mM or 1.7 mM $MgCl_2$). Samples (360 μl) were

542 loaded into 12 mm charcoal-filled epon double sector centerpieces. A rotor speed of 22,000 rpm was

543 selected and absorbance optics scans at a wavelength of 258 nm were collected every second until

544 sedimentation was complete. Data were analyzed using the c(s) model in SEDFIT which directly models

545 the sedimentation boundary as a continuous distribution of discrete, non-interacting species (Schuck,

546   2000). Buffer density and viscosity as well as sample partial specific volumes were calculated using

547   UltraScan III (Demeler & Gorbet, 2016).

548   **Negative stain electron microscopy**

549   Quantifoil R2/1 Cu200 C2 grids were plasma cleaned for 20 s at 20 mA (GloCube, Quorum). 3.5 µL of

550   sample containing 1-4 ng/µL (0.3-1.3 nM) of 25mer in buffer (3 mM Tris-HCl pH 8.0, 0.03 mM EDTA pH

551   8.0, 0.03 mM DTT, 50 mM NaCl, 0.2/1.7 MgCl$_2$) was applied, incubated 30 s, then hand blotted. Grids

552   were negative stained with 2x 3.5 µL of 2% uranyl acetate, and hand blotted after 30 s for each stain

553   application. Images were collected using an FEI Morgagni 100 keV TEM with a SIS Megaview III 1k CCD,

554   at a nominal magnification of 56,000x.

555   *Analysis of electron micrographs*

556   Outlines of single particles were determined with a trainable Weka segmentation in ImageJ (Fiji).

557   Feret´s diameter (the maximum distance between two parallel tangential lines), and circularity were

558   calculated for this outline using equation 1.

$$circularity = \frac{4\pi * area}{perimeter^2}$$

559   (Eq. 1)

560   **Restriction based nucleosome sliding assay**

561   Remodeling assays contained 4 nM 25mer arrays (100 nM total nucleosome concentration), 200 nM

562   ISWI, ATP regeneration system (6 mM phosphoenolpyruvate, 15.5 U/mL pyruvate kinase/lactate

563   dehydrogenase, 1 mM DTT), indicated magnesium concentration and 5 µM Mg-ATP in remodeling

564   buffer RB (25 mM Hepes pH=7.6, 0.1 mM EDTA, 50 mM NaCl, 10% (v/v) glycerol, 0.2 mg/mL BSA).

565   Beforehand, chromatin arrays were dialyzed overnight into 10 mM Tris pH=7.6 at 4 °C. The reaction

566   was started with addition of ISWI and incubated at 26 °C. At different time points, 20 µL aliquots were

567   taken and remodeling was quenched with apyrase (50 mU, 1 min, 26 °C). The Mg^{2+} concentration was

568 supplemented to a final concentration of 1.7 mM $MgCl_2$ for all samples. Samples were digested with

569 10 U/125 ng array of BamHI for 90 min at 26 °C. The digestion was stopped with addition of 20 mM

570 EDTA and 0.5% SDS, followed by Proteinase K (final concentration 0.5 mg/mL) treatment for three

571 hours at 37 °C. Samples were ethanol precipitated and separated on an agarose gel (0.7% to 0.9% in

572 0.5xTBE, 20 cm). Gels and running buffers contained 0.5 µg/mL EtBr. The bands were analyzed with

573 *AIDA Image Analyzer Software* and the percentage of *Cut*-DNA calculated. The dependence of

574 percentage of Cut-DNA versus time was fitted in R into to a single exponential function (Eq.2):

575 $$\%cut = \%cut_{max} * (1 - e^{-kobs*t}) \hspace{3cm} (Eq.\ 2)$$

576 **ATPase assay**

577 A NADH-oxidation coupled ATPase assay was performed as described (Mueller-Planitz et al., 2013).

578 Briefly, 30 µl reactions were assembled on a 384-well plate (Greiner, 781101), containing 100 nM ISWI

579 and 0.1/0.5/1.33 µM mononucleosomes (0N60) in remodeling buffer supplemented with ATP-

580 regeneration system and 0.6 mM NADH. Each sample was measured in technical triplicates. Reactions

581 were started by addition of 1 mM Mg-ATP and NADH absorbance was monitored at 340 nm in a plate

582 reader (Biotek PowerWave HT) at 26°C. Absorbance readings between ten and 20 minutes were fit to

583 a linear function.

584 **Phase separation of nucleosome arrays and imaging of formed chromatin condensates**

585 All phase separation experiments were performed in phase separation buffer (PSB) (25 mM Hepes-

586 KOH pH 7.6, 0.1 mM EDTA, 50 mM NaCl, 10% glycerol, 1 mM DTT, 0.2 g/L BSA) supplemented with 1

587 mM $MgCl_2$ (PSB1) or 5 mM $MgCl_2$ (PSB5). Phase separation was induced by mixing equal volumes of

588 nucleosome arrays diluted in TE buffer with 2x PSB. The formed chromatin condensates (4-10 µL of

589 sample) were incubated at room temperature for a minute and then loaded onto the imaging chamber

590 made out of double-sided tape. Double-sided tape was pierced with a hole puncher before and sample

591   was deposited into the hole. Cover slips were pretreated with 20 µL of BSA solution (25 mM Hepes-

592   KOH pH 7.6, 0.1 mM EDTA, 50 mM NaCl, 10% glycerol, 1 mM DTT, 100 mg/mL BSA) for one minute.

593   The imaging chamber was sealed with nail polish, and unless stated otherwise, spun onto the cover

594   slip (1 min, 1000g, room temperature). Samples we then imaged on a widefield microscope (Zeiss

595   Axiovert).

596   *Analysis of phase diagram*

597   Condensates were detected by Trainable Weka segmentation in ImageJ, their surface was calculated

598   as a percentage of a total field of view surface and plotted in form of a heatmap in R.

599   **Confocal imaging**

600   Confocal and FLIM images were performed with a TCS SP8 X FALCON confocal head (Leica

601   Microsystems, Wetzlar, Germany) mounted on an inverted microscope (DMi8; Leica Microsystems).

602   For confocal imaging, a white light laser was used as excitation source (561 nm or 633 nm as

603   necessary). Single photons were collected through a 40×/1.3 NA oil-immersion objective and detected

604   on Hybrid Detectors (HyD) (Leica Microsystems) with a 570 − 610 nm, and 650 − 707 nm spectral

605   detection window as necessary. Sequential excitation was performed to avoid potential crosstalk

606   between the fluorophores.

607   **FITC-dextran partitioning in chromatin condensates**

608   Condensates were formed in a solution containing 100 nM 13mer (final concentration 90 nM), PSB2

609   supplemented with 2.5 mM DTT and incubated for five minutes at room temperature when the FITC-

610   dextrans (Sigma) diluted in water were added to final concentration of 0.1 mg/mL. Samples were

611   prepared as described above and imaged on Leica laser scanning confocal microscope after 1 h

612   incubation at room temperature.

28

613   Images were analyzed in ImageJ, where the dextran partitioning coefficient was determined for

614   individual condensates as a ratio of fluorescence inside the condensate and background fluorescence.

615   Molecular weights of dextrans were converted into Stokes radii with an online tool

616   (https://www.fluidic.com/toolkit/hydrodynamic-radius-converter/).

617   **ISWI colocalization experiment**

618   Chromatin and ISWI colocalization experiment was performed with 40 nM of unlabeled 25mer, 10 nM

619   of 25mer-Cy3 and 1.125 µM ISWI-GFP/GFP-GST in PSB5. Condensates were induced by adding Mg^{2+}

620   (5 mM) either after or before addition of GFP-GST or ISWI-GFP.

621   A standard curve for mean Gray value dependence on ISWI-GFP concentration was obtained from

622   ISWI-GFP dilutions in PSB5. Different microscope settings were used to image lower and higher

623   dilutions. ISWI-GFP concentration was then determined inside condensates and in a surrounding

624   solution for 90 nM 13mer, 234 nM ISWI-GFP, 1 mM Mg-ATP, ATP-regeneration system, PSB1 and for

625   45 nM 25mer, 125 nM 0N60 mononucleosomes, 625 nM ISWI-GFP, 1 mM Mg-ATP, ATP-regeneration

626   system, PSB5.

627   **Restriction enzyme accessibility nucleosome sliding assay adapted to chromatin condensates**

628   A *KpnI* site was used to compare nucleosome sliding in 25mer arrays fully dissolved or after

629   condensate separation. A remodeling assay contained 15 nM 25mer, 750 nM ISWI, ATP regeneration

630   system and 1 mM Mg-ATP in PSB0.2/5, in total reaction volume of 20 µL. Reaction was started with 2

631   µL of ISWI (Fig. 2d) or ATP (Fig. S2c) and incubated at 26 °C. Before the reaction was started, 6 µL of

632   the reaction mixture were checked under the microscope for chromatin condensates. At different

633   time points, 1 µL of reaction was quenched with 45 µL of quenching solution (10 mU/µL apyrase in

634   apyrase reactions buffer, containing 1.8 µL 2 mM $MgCl_2$ for low magnesium reactions), incubated at

635   26 °C for 15 min and after that kept on ice. After all time points were quenched, the reaction mixture

636   was again checked under the microscope for the presence of condensates. To each tube, 2.5 μL of

637   *KpnI* was added and incubated at 26 °C for 30 min. Cleavage was detected as above for the restriction-

638   based nucleosome sliding assay, except that ImageJ was used for quantification.

639   **FLIM-FRET**

640   *Slide preparation*

641   For end point assays (Fig. 2f), 45 nM 25mer (1125 nM nucleosome concentration), 125 nM labeled

642   mononucleosomes, 625 nM ISWI, ATP regeneration system and 1 mM Mg-ATP were mixed in PSB5 in

643   total volume of 10 μL. Samples were incubated at room temperature for 15 minutes, 6 μL was

644   transferred on a slide (see above for slide preparation), spun as above, and imaged after four hours.

645   For time lapse assays (Fig. 2g), 40 μL of the reaction mixture was loaded into the channel of imaging

646   chamber (Ibidi μ-Slide VI$^{0.5}$ Glass Bottom 80607). The imaging chamber was spun down and mounted

647   on the microscope. Lifetimes were measured for two min before addition nucleotides. Then, 120 μL

648   of 1 mM Mg-ATP or 1 mM Mg-AMPPNP solution, dissolved in identical buffer and supplemented with

649   ATP regeneration system, was filled into one of the reservoirs without removing the chamber from

650   the microscope or stopping the imaging. Nucleotide solution then replaced solution above the

651   condensates by gravity flow. Time lapses were recorded for two h. Finally, time lapses in Fig. 2h and

652   Fig. S2h contained 1125 nM unlabeled mononucleosomes or 45 nM 25mer, 125 nM FRET

653   mononucleosomes and ATP regeneration system in PSB5 in total volume of 18 μL. Two μL of 10x Mg-

654   ATP solution were added to a final concentration 1 or 5 mM, the mixture was loaded into a channel

655   of the imaging chamber and imaged two to four min after ATP addition.

656   *Image acquisition*

657   For FLIM, the same system described in "Confocal Imaging" was used. The white light laser delivered

658   80 MHz repetition rate at 561 nm. Arrival time of single photons was measured with the included

659   FALCON module. The FLIM acceptor photobleaching image kept the same parameters as the confocal

660   one with 12 frames accumulations instead. The other FLIM images and movies size was set to 256 ×

661   256 pixels. A 3-fold zoom factor was applied, giving a pixel size of 0.380 μm and an image size of 97 ×

662   97 μm. Pixels number was decreased to favor imaging speed in the time-lapses. Because the statistical

663   determination of the distribution of single photon arrival times requires a minimum number of

664   photons, 60 frames were acquired at 2.34 Hz for each TCSPC recording, for a total time of around 26

665   s. Corresponding to a scanning speed of 600 Hz. Time-lapses were recorded for at least 15 min with a

666   time point every 2 min.

667   *Analysis*

668   FLIM image analyses were performed in the LAS X software and with a home-made MatLab code

669   (available on request). Lifetime calculations were based on the Phasor approach (Digman et al., 2008).

670   Phase and modulation lifetimes were calculated using the Fourier sine and cosine transforms of the

671   lifetime images. The FRET efficiency (E$_{FRET}$) was calculated according to Eq. 3:

672    $$E_{FRET} = 1 - \frac{\tau_{DA}}{\tau_D} \qquad \text{(Eq. 3)}$$

673   where τ$_{DA}$ is the lifetime of the donor-acceptor sample, and τ$_D$ is the lifetime of the donor alone. Results

674   were expressed as mean ± SD. Lifetimes images shown were done using the phasor approach to

675   maximize the number of photons while keeping a good image resolution. For the time lapse, the linear

676   part of lifetime changes was fitted to a linear function to obtain initial velocity.

677   **Holotomography**

678   Slide with 25mer condensates containing ISWI in PSB5 buffer was prepared as described above.

679   Refractive index images were collected on 3D Cell Explorer-fluo (Nanolive) equipped with dry objective

680   (60x magnification, 0.8 numerical aperture) and low power laser (λ = 520 nm, sample exposure 0.2

681 mW/mm$_2$). 96 slices were collected for a field depth of 30 μm. Software Steve v.1.6.3496 (Nanolive)

682 was used to collect, view and export images. Data were exported as tiff files (floating values of RI) and

683 further processed in ImageJ (Fiji). Eq. 4 was used to calculate chromatin mass concentration in

684 condensates, where n = refrective index, c = mass concentration and dn/dc is a refractive index

685 increment. We assumed $c_{condensate} \gg c_{solution}$ and dn/dc to be 0.185 mL/g.

686 $$n_{condensate} - n_{solution} = \frac{dn}{dc} * (c_{condensate} - c_{solution}) \qquad \text{(Eq. 4)}$$

687 **ISWI-GFP and 25mer-Cy3 FRAP**

688 Four μL of 2.5x mixture of unlabeled chromatin, labeled chromatin and ISWI-GFP were mixed with six

689 μL 1.7xPSB5 containing 1.7xnucleotide. Final experimental conditions were: 76 nM 25mer, 1.75 nM

690 Cy3-25mer, 1 μM ISWI-GFP, 0.77 mM Mg-nucleotide, PSB5, ATP regeneration system (Fig. 3b); 15 nM

691 25mer-Cy3, 375 nM ISWI-GFP, PSB5, 1 mM Mg-ATP/no nucleotide (Fig. S3a); 100 nM 25mer, 4.5 nM

692 25mer-Cy3, 1.3 μM ISWI-GFP, PSB5, ATP regeneration system, 1 mM Mg-ATP (Fig. S3b). The sample

693 was incubated for 1 min and then loaded onto the slide, spun, sealed as above and imaged within 30

694 minutes of preparation.

695 Images were acquired at 26°C with a 63X glycerol immersion objective on a Leica Sp5 confocal

696 microscope equipped with Argon 488 nm and DPSS 561 nm lasers. For ISWI-GFP FRAP, 10 frames

697 (512x512 pixel) at 1.2 s intervals were taken as a pre-bleach reference, followed by a single 1.2 s

698 bleaching pulse targeted to a circular region within ≥ 3 droplets at once. After bleaching, 89 frames

699 were taken at 1.2 s intervals to measure fluorescence recovery. For H4-Cy3 FRAP, 10 frames (512x512

700 pixel) at 1.2 s intervals were taken as pre-bleach reference, followed by four 1.2 s bleaching pulses

701 targeted to a circular region within ≥ 3 droplets at once. After bleaching, 20 frames were taken at 30

702 s intervals to measure fluorescence recovery. For both cases, brightfield images were also collected in

703 parallel.

704   All images were processed using Fiji (Schindelin et al., 2012). First, drift was corrected using

705   MultiStackReg package (https://biii.eu/multistackreg) by calculating transformation matrices from

706   brightfield images (code available on request). Bleach, control (within droplet but outside the

707   bleached region) and background Region Of Interest (ROIs) were manually defined, and average

708   fluorescence intensity was measured. Intensities were normalized using the easyFRAP web tool

709   (Koulouras et al., 2018) to generate FRAP curves with full scale normalization. Normalized FRAP curves

710   from different droplets within the same experiment were considered as technical replicates. FRAP

711   curves from different experiments were averaged and reported together with standard error of the

712   mean (SEM). Plots were generated using R – version 4.2.1 (https://www.R-project.org/) (R Core Team,

713   2022).

714   **Controlled condensate fusion with optical tweezers**

715   Four µL of chromatin ISWI mixture (225 nM 13mer, 585 nM ISWI, volume was made up with TE pH=7.6)

716   was gently mixed with 6 µL 1.7xPSB1 containing 1.7xnucleotide. Final experimental conditions were:

717   90 nM 13mer, 234 nM ISWI, 1 mM Mg-nucleotide and ATP regeneration system in 1xPSB1. Data on

718   fusion velocity with different ISWI concentrations (Fig. S3e) were collected in 1xPSB1 supplemented

719   with 5 mM DTT. Of note, with an ATP-regeneration system present, slow fusion was detected with

720   AMPPNP and ADP-BeF$_x$, presumably due to ADP contamination present in nucleotide preparations.

721   Samples were incubated for 1 min and then loaded onto prepared slides. Optical tweezer experiments

722   were carried out on a dual-trap C-Trap (Lumicks, Amsterdam). For controlled fusion of condensates, a

723   single condensate was trapped in each of the optical traps at minimal laser power, resulting in trap

724   stiffnesses on the order of ~0.001 pN/nm. The traps were approached in 20 nm steps until the

725   condensates touched and fusion started which was determined by observation of a rapid drop in the

726   force signal (Fig. S3c). During fusion, the trap distance was then held constant. Fusion was further

727   monitored by brightfield microscopy. Events in which fusion was not complete after 30 s were counted

728   as non-fusing and assigned a fusion velocity of 0.

729   Analysis was performed using custom written code for the IGOR Pro 8 software (WaveMetrics, USA).

730   Fusion velocity was determined by fitting a generalized logistic function (Eq. 5) to the differential force

731   data along the x-axis. With F(start) and F(finish) the differential forces before fusion onset and after

732   finished fusion, respectively.

733   $$F(x) = F(finish) + \frac{F(start) - \text{F}(finish)}{1 + e^{\left(\frac{t-t_0}{\tau}\right)^{\gamma}}}$$ (Eq. 5)

734   The force was then normalized so that F(start) = 0 and F(finish) = 1. The fusion velocity was determined

735   as the slope of the tangent fitted to the normalized force data at the inflection point of the fitted

736   function. As the fusion velocity is inversely proportional to the size of the condensates, the obtained

737   velocity was normalized using the mean size of the two fused condensates which was obtained using

738   radial profiling of the brightfield videos pre-fusion. For comparison between conditions velocities were

739   transformed into the log10-fold change relative to the mean of the chromatin only condition.

740   Statistical significance of the velocity changes was determined by t-test. Data is visualized in boxplots

741   showing the median ± quartiles, with whiskers indicating the 9th and 91st percentile.

742   **ThT fluorescency measurment**

743   Thioflavin T (ThT) fluorescence intensity was measured with increasing ISWI concentrations with 90

744   nM 13mer in modified PSB (supplemented with 2 mM $MgCl_2$, 2.5 mM DTT and 40 µM ThT).

745   **Molecular dynamics simulations**

746   Molecular dynamics simulations were performed using custom written software in C++ and CUDA.

747   Chromatin arrays were described as Rouse chains with an equilibrium distance between nucleosomes

748   of 16 nm and a spring constant of 15 pN/nm. All nucleosome particles further interacted with each

749   other via truncated Lennard-Jones potentials. The remodeler was modeled as single particles that

750   repel each other and can form two independent interactions with nucleosomes (Fig. S4a). All particle

751   interactions were described as truncated Lennard-Jones potentials with an equilibrium distance of 16

752   nm and a cutoff distance of 48 nm. Between 32 and 48 nm the potential was simplified using a linear

753   approximation (Fig. S4c). The strength of the remodeler-nucleosome interactions was modulated

754   based on the remodeler's nucleotide state. The first interaction site switched from a remodeler off-

755   rate of $2.5*10^{-6}$ timestep^{-1} in the nucleotide-free state to an off-rate of $1.25*10^{-7}$ timestep^{-1} in the ATP

756   and ADP bound states. The second interaction site had a remodeler off-rate of $1.25*10^{-6}$ timestep^{-1} in

757   the ADP bound state and $1.25*10^{-7}$ timestep^{-1} in the ATP bound state and without bound nucleotide.

758   Condensates were formed from 169 Rouse chains of length 13 and 440 remodeler particles that were

759   equilibrated in their respective nucleosome condition for $4*10^7$ timesteps before use in FRAP or fusion

760   simulations. Particle motion was modeled using the Langevin equation with a diffusion coefficient of

761   0.02 nm^2/timestep ($8*10^5$ nm²/s) corresponding to remodeler diffusion *in vivo* (Kim *et al.*, 2021) in

762   timesteps of 20 ns.

763   Apart from simplifications due to coarse-graining, the prime reason why we achieve only qualitative,

764   rather than quantitative agreement between the coarse-grained simulations and experiments lies in

765   technical constraints required for computational performance. To keep the simulation tractable,

766   typical simulated droplet sizes are approximately an order of magnitude smaller than their

767   experimental counterparts. Even in the model of ISWI being a stable crosslinker, a small shape change

768   during droplet fusion may be expected from the stretching of arrays. This relative change is much

769   more pronounced for the smaller simulated droplets, compared to the experimental droplets. In

770   addition, simulated fusion trajectories have a well-defined endpoint (circularity=1), such that we were

771   able to determine a fusion velocity for all simulation trajectories. In contrast, the fusion velocity for

772   experimental trajectories could only be determined for events which completed fusion (see previous

773   section).

Simulated FRAP

775   For the simulation of FRAP experiments, remodeler particles in one half of the condensate were

776   marked as bleached. Mixing was determined using the distances between particles. First, pairwise

777   distances either between all particles of one type ($dist_{all}$) or only between bleached and non-bleached

778   particles ($dist_{cross}$) were determined.

779   The pairwise distances were binned, and mixing (M) was quantified with Eq.6

780    $$M = \sum \frac{(dist_{cross} - dist_{all})^2}{dist_{all}} \qquad \text{(Eq.6)}$$

781   This was done at timesteps $2.5*10^6$ timesteps apart. The resulting values were normalized between 0

782   and 1 to emulate FRAP recovery. For each condition three simulations were performed. Data was

783   visualized in boxplots showing the median ± quartiles and whiskers showing the maximum and

784   minimum values.

Simulated fusion

786   For the simulation of condensate fusion, two preequilibrated condensates were positioned in close

787   proximity. Fusion progress was then measured using the sphericity of the system over time which

788   approaches 1 as fusion progresses. The circularity was then fitted with the same generalized logistic

789   function as the force response in the experiments. Three simulations were performed for each

790   condition. Relative fusion velocities were obtained by normalizing the data to the mean of the

791   nucleotide free condition. Data was visualized as boxplots as described for simulated FRAP.

Acknowledgements

801   **Author contributions.**

802   Conceptualization: F.M.-P., J.S., P.V.

803   Methodology and formal analysis: P.V., J.S., M.G.P, N.H., A.S., D.K., M.S.

804   Investigation: P.V., M.G.P., A.S., J.B., J.S., D.K., N.H., M.S.

805   Writing of original draft: F.M.-P., P.V., M.G.P, D.K., M.S., A.S., J.B., J.S.

806   Visualization: P.V., J.S., D.K., M.S., M.G.P.

807   Funding acquisition: F.M.-P., J.S., P.B.B, M.H.

808   Writing—Review and Editing: All authors

809   **Data availability statement.**

810   Authors can confirm that all relevant data are included in the article and/or its supplementary

811   information files.

812   **Code availability statement.**

813   Code available on request from the authors. The MD simulation executable as well as analysis

814   scripts for MD simulations and controlled condensate fusion experiments are available at

815   https://github.com/StiglerLab/Vizjak_2023.

816

817
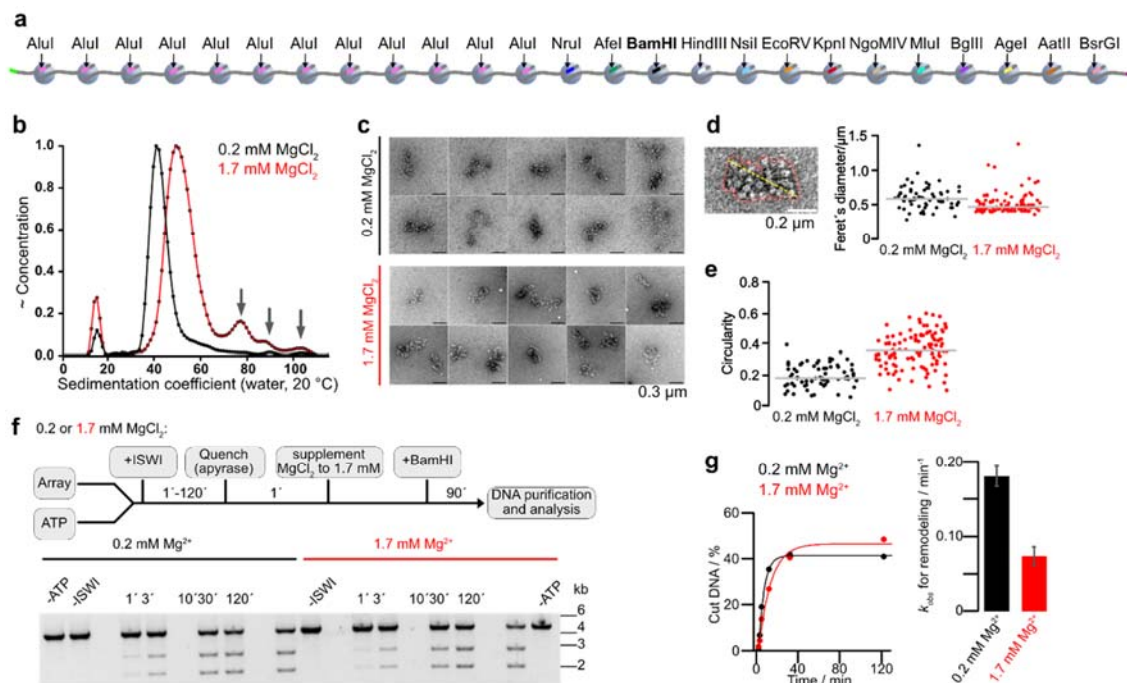
Figure 1. Intramolecular chromatin fiber folding does not impede remodeling. a, A 25mer nucleosome array assembled on 25 repeats of 197 bp long Widom-601 DNA derivatives. 13 repeats contain unique restriction enzymes sites. **b**, Sedimentation velocity analysis of 25mer arrays in a buffer supplemented with 0.2 mM (black; peak at 42.4 S) or 1.7 mM MgCl$_2$ (red; peak at 51.3 S). The larger S value at the higher Mg^{2+}-concentration indicated stronger compaction of arrays without substantial oligomer formation (arrows). **c**, Representative micrographs of 25mer arrays from negative stain electron microscopy dissolved in a buffer supplemented with indicated MgCl$_2$ concentrations. **d**, **e,** Single-particle analysis of negative stain EM micrographs. N = 67 (0.2 mM MgCl$_2$); N = 107 (1.7 mM MgCl$_2$). Outlines of single particles (red line) were determined with a trainable Weka segmentation in ImageJ. Feret´s diameter (the maximum distance between two parallel tangential lines, yellow line) and circularity were calculated for all outlines. **f**, Top: Schematic of the BamHI accessibility assay. Bottom: Gel analysis of remodeling time courses. Reactions contained 4 nM arrays and 5 µM Mg-ATP and were started by addition of 200 nM ISWI. **g**, Left: quantification of gel in *f* and exponential fits of the time courses. Right: rate coefficients from single exponential fits. Bars are mean values of two independent experiments, error bars their minimal and maximal values.
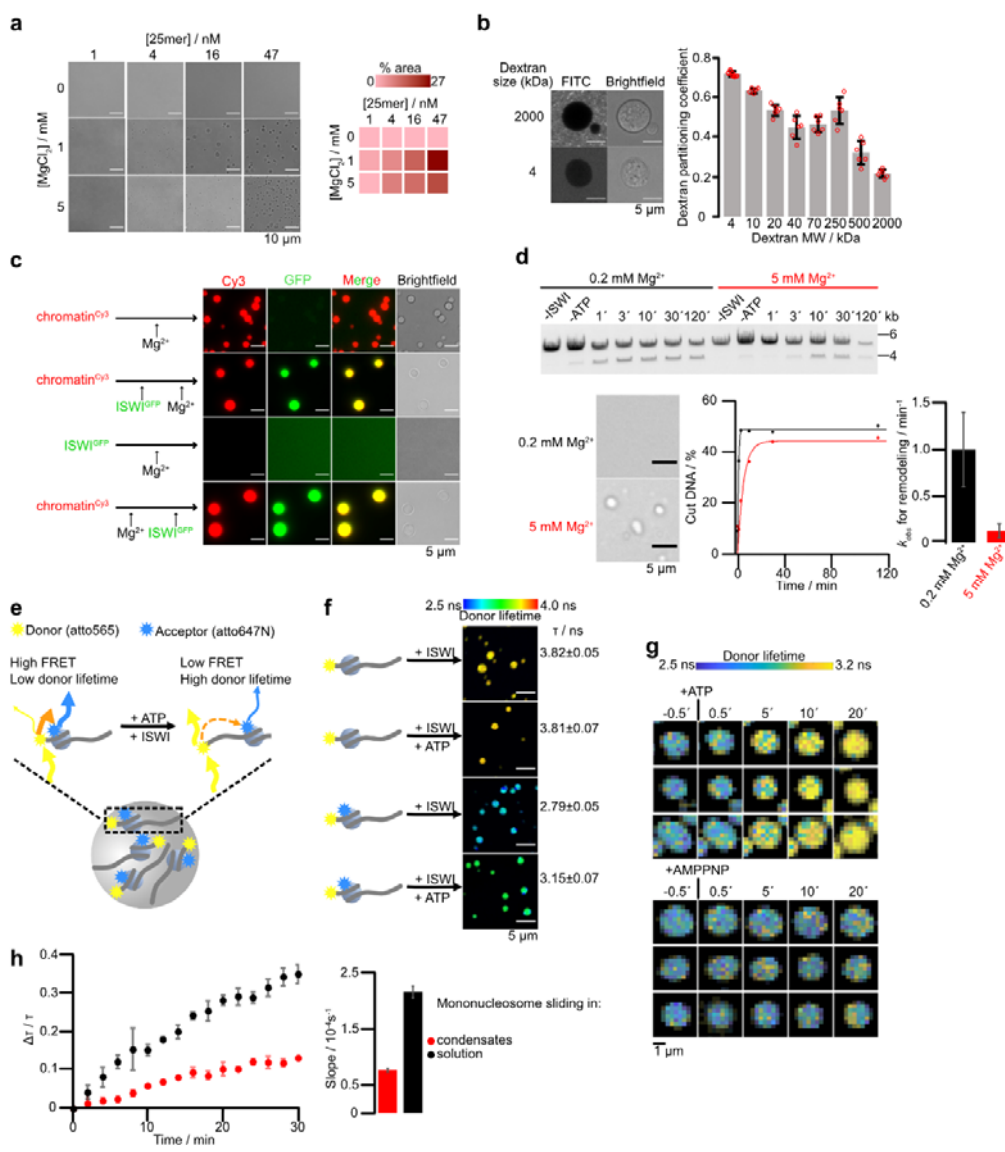
Figure 2. ISWI slides nucleosomes inside chromatin condensates. a, Condensate formation depends on nucleosome and $MgCl_2$ concentration. Left: Condensate formation for different $MgCl_2$ and 25mer array concentrations. Right: Percentage of the field of view occupied by condensates. **b**, Partition coefficient of FITC-labeled dextrans of indicated molecular weights. Bars are averages from six condensates for each dextran, errors are SD. **c**, Colocalization experiments with GFP-ISWI (1.1 µM) and Cy3-labeled condensates (0.05 µM 25mers). Condensates were induced by addition Mg^{2+} (5 mM) either before or after addition of GFP-ISWI. **d,** Nucleosome sliding time courses (top and bottom left) in absence and presence of condensates (bottom right). Sliding was measured by KpnI accessibility of 25mer arrays (15 nM) with 1 mM Mg-ATP. Reactions were started by addition of 750 nM ISWI. Bars are mean values of two independent experiments, error bars their minimal and maximal values. **e,** Principle of the FLIM-FRET sliding assay. FRET nucleosomes with a donor dye (atto565) coupled to H2A K119C and an acceptor dye (atto647) attached to the octamer-proximal end of 207 bp Widom-601 DNA were spiked to array condensates. Upon nucleosome sliding, the FRET efficiency decreases, prolonging the donor fluorescence lifetime. **f,** The donor lifetime of FRET-nucleosomes in condensates

848 increased after addition of ISWI and Mg-ATP but not in negative controls (donor-only nucleosomes,
849 or without Mg-ATP). One out of two independent replicates with similar results is shown. Bars are
850 averages and error bars are SD of lifetimes across ten fields of view of the same sample, with each
851 field of view imaged 30 times, totaling 300 images per condition. Reactions contained 45 nM 25mers,
852 125 nM FRET nucleosomes, 625 nM ISWI and were imaged four hours after addition of Mg-ATP. **g,**
853 FLIM time lapse microscopy. Mg-ATP or Mg-AMPPNP (both 1 mM) were flown into the imaging
854 chamber at t = 0. Individual condensates are pictured. One of two independent replicates with similar
855 results is displayed. **h,** Left: FLIM-FRET time courses in condensates (N=3) and solution (N=2). Points
856 are mean values of independent experiments, error bars their minimal and maximal values.
857 Condensate reactions contained 45 nM 25mers, 125 nM FRET nucleosomes, and 625 nM ISWI and
858 were started with 1 mM Mg-ATP. Solution reactions contained 1125 nM unlabeled 0N60 nucleosomes
859 instead of arrays. Right: Initial velocities of time courses obtained from linear fits of the time courses.
860 Bars are mean values of independent experiments, error bars their minimal and maximal values.
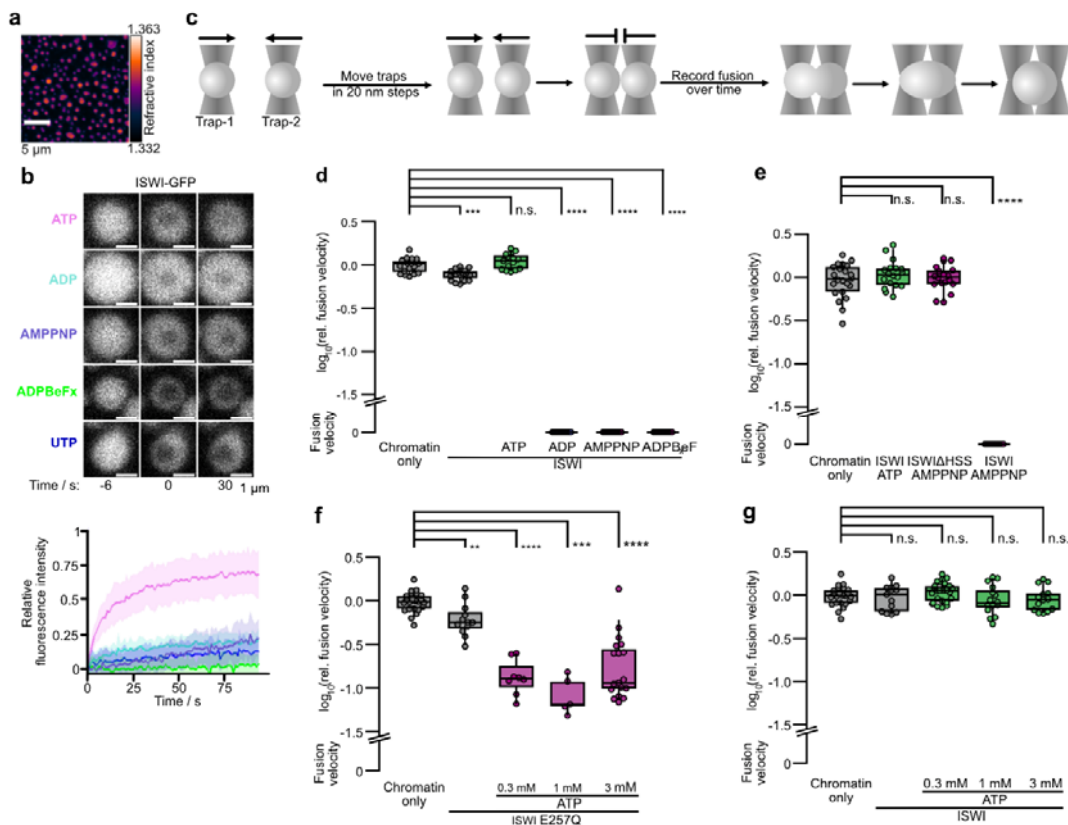

861

862 **Figure 3. ATP hydrolysis powers mobility of ISWI and prevents ISWI-mediated hardening of**
863 **condensates. a**, Holotomogram of chromatin condensates. The average nucleosome concentration
864 (225 ± 59 μM) was determined from the refractive index. One of two independent replicates is
865 depicted. **b,** Left: Partial-condensate FRAP of ISWI-GFP in presence of indicated nucleotides (all 0.77
866 mM). Only the addition of ATP allowed a fast recovery. Bottom: Quantification of FRAP time courses.
867 Lines are averages, shaded areas SD of 20 condensates for AMPPNP and UTP, 15 for ADP, 25 for ADP-
868 BeF$_x$ and 30 for ATP. **c,** Schematic of condensate fusion experiments with optical tweezers. **d,** Fusion
869 velocities of condensates measured by optical trapping. ISWI in presence of non-hydrolysable
870 nucleotides but not of ATP, slowed down fusion. Chromatin-only and nucleotide-free ISWI conditions

871   were replicated three times. **e,** AMPPNP did not slow down fusion when ISWI lacked its HSS domain.
872   **f,** Addition of ATP to an ATPase dead mutant of ISWI (E257Q) slowed down condensate fusion. **g,**
873   Addition of ATP to wild type ISWI did not affect condensate fusion. Data in d–g are log10-fold changes
874   in velocities relative to the mean of the chromatin only condition. Unless stated otherwise, all data
875   were independently replicated twice per condition.

876
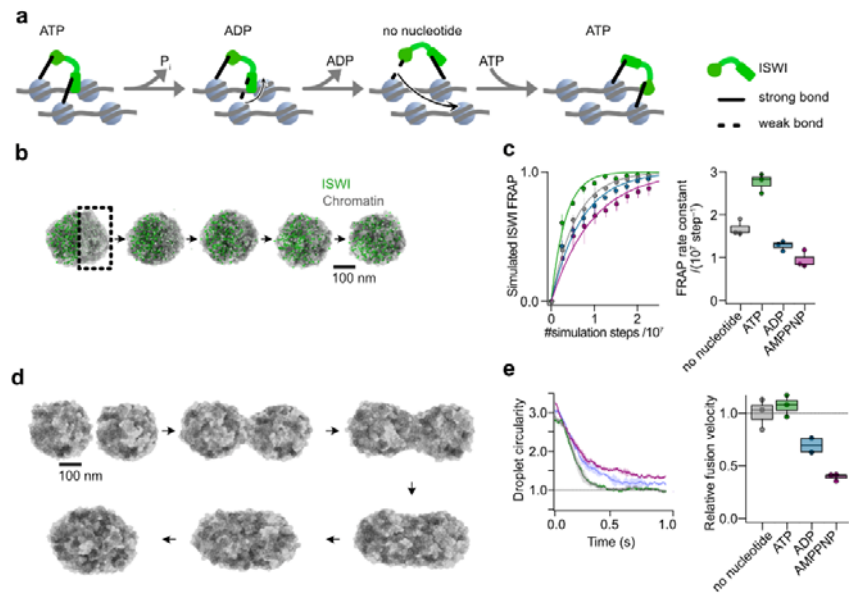
Figure 4. A simple model qualitatively explains experimental observations. a, ISWI possesses two nucleosome-interacting domains, which can bridge neighboring nucleosomes in dense chromatin. Via large nucleotide-induced conformational changes (not shown), the domains cycle through high and low affinity states towards nucleosomes, allowing ISWI to actively translocate through chromatin. **b,** Representation of a molecular dynamics simulation of ISWI FRAP in a chromatin condensate. ISWI particles on one side of an equilibrated condensate are switched to a bleached state at t=0 (square). Particle dynamics are then simulated to observe mixing of the two ISWI populations. **c,** ISWI FRAP was simulated as in b for $2.25*10^7$ timesteps in different nucleotide conditions with three replicates per condition. Left: Averaged traces of ISWI FRAP in different nucleotide conditions. Right: Rate constants of the simulated FRAP traces. **d,** Representation of simulated fusion experiments. Two equilibrated condensates were brought into proximity and allowed to fuse. For visual clarity only nucleosomes are shown here. **e,** Simulations of three fusion events for each nucleotide condition. Left: Averaged fusion traces with standard error. Right: Relative fusion velocities of the simulated traces.

890
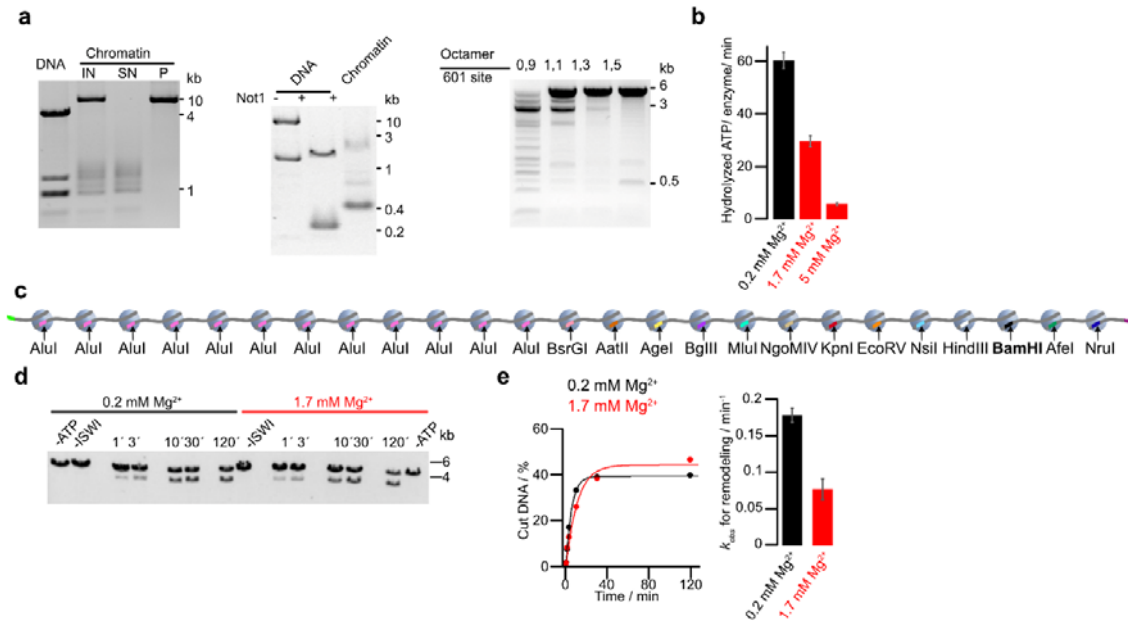
Figure S1. a, Quality controls for 25mer nucleosome arrays. Left: agarose gel after magnesium precipitation of assembled arrays and the resolubilized pellet. IN, input; SN, supernatant; P, pellet. Competitor DNA derived from the plasmid backbone (< 1 kb) was excluded from P. Middle: Not1 digestion (a Not1 site is present in each linker) liberated mostly mononucleosomes, running around 400 bp, but little 197 bp fragments, confirming saturation of most 601 repeats with octamers. Right: BsiWI digestion (all nucleosomes occlude a BsiWI restriction site) for arrays assembled with different octamer amounts. As 601 sites become saturated, digestion is hindered. **b**, ATP turnover in the presence of saturating concentrations of mononucleosomes (1.33 µM). Control experiments with three times lower mononucleosome concentrations gave the same results. Bars are mean values of two independent experiments, error bars their minimal and maximal values. Increasing Mg-concentrations reduce mononucleosome-stimulated ATP hydrolysis rates at saturating concentrations of ATP (1 mM). **c**, As in Fig. 1a, but with different orientation of the unique restriction sites such that the BamHI site is now more peripheral. **d**, BamHI accessibility assay as in Fig. 1f but for the array shown in *c*. **e**, Left: quantification of gel in *d* and exponential fits of time courses. Right: rate coefficients from single exponential fits. Bars are mean values of two independent experiments, error bars their minimal and maximal values.
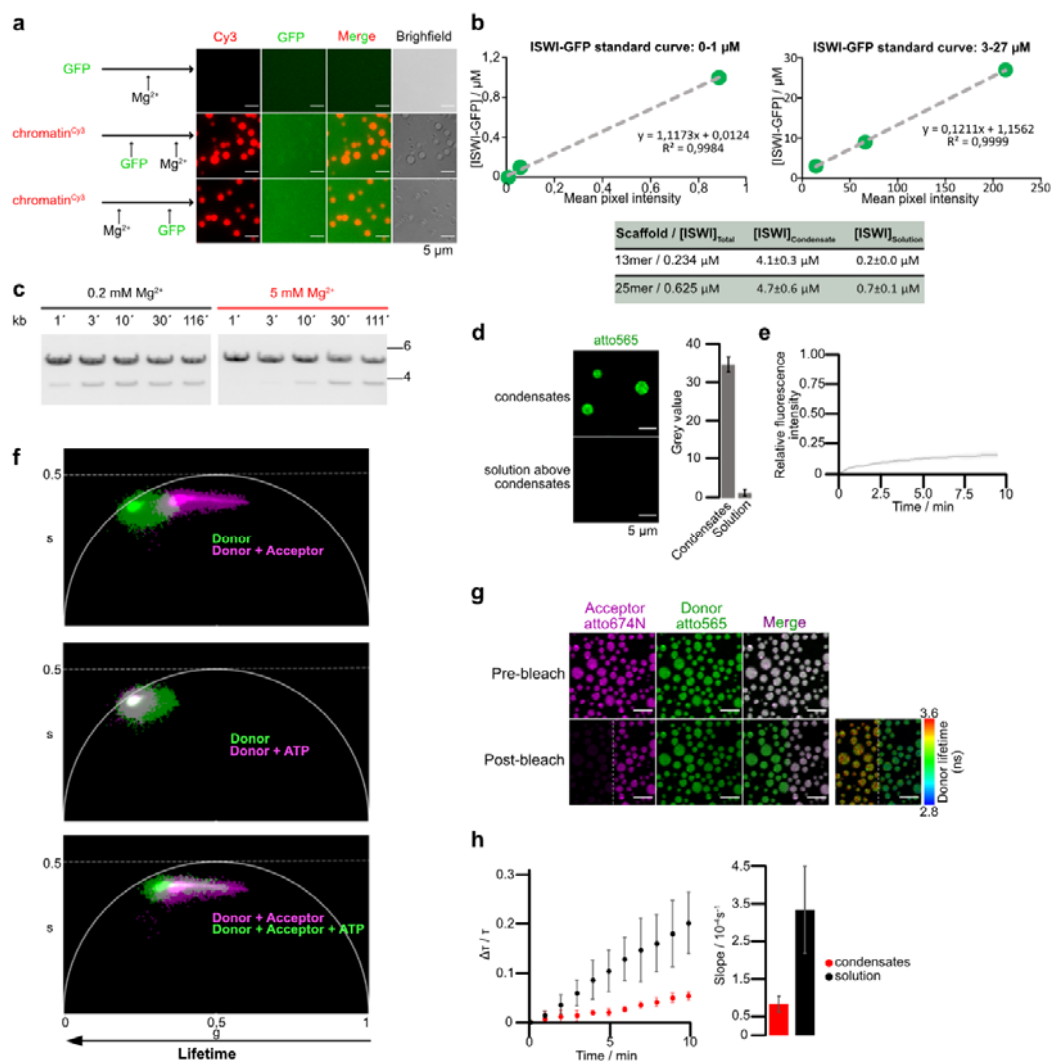
Figure S2. a, GFP does not partition into chromatin condensates. The colocalization experiment was performed with 40 nM of unlabeled 25mer, 10 nM of 25mer-Cy3 and 1.125 µM of GFP-GST. **b,** ISWI-GFP concentrations were determined inside condensates and, after centrifugation, in the surrounding solution (bottom) from fluorescence intensities using calibration curves with ISWI-GFP dilutions (top). Two different microscope settings were used to image lower and higher dilutions. Means and SD of two independent replicates are shown. **c,** Nucleosome sliding time courses in absence and presence of condensates (0.2 mM and 5 mM $MgCl_2$, respectively), replicate of experiment in Fig. 2e. Sliding was measured by KpnI accessibility of 25mer arrays (15 nM). Reactions contained 750 nM ISWI and were started by addition of 1 mM Mg-ATP. **d,** Enrichment of labeled 0N60 mononucleosomes in chromatin condensates, N = 3 ± SD. The mononucleosome concentration in solution was determined from z-plane above the condensates. **e,** Whole condensate FRAP of FRET-0N60 nucleosomes to assess their exchange between condensate and solution. Line is an average and shadow SD of eight bleached condensates. One of four independent replicates with similar results is shown. **f,** Phasor representation of data in Fig. 2f. The phasor representation makes no assumptions on the number of decay rates nor on specific decay model (exponential, non-exponential) (Digman et al., 2008). Upon

45

923   introduction of the acceptor, the donor's lifetime distribution moves away from the universal circle
924   line (single exponential lifetimes). This is consistent with an existence of at least two or even three
925   different populations of donor: high FRET, low FRET and no FRET. **g,** Acceptor bleaching enhances
926   donor fluorescence and lifetime, indicative of FRET. Imaging of FRET-0N60 nucleosomes in chromatin
927   condensates. The acceptor fluorophore was bleached in the left half of the field of view, leading to an
928   increase in donor fluorescence and donor lifetime (right most panel). **h,** FLIM-FRET measurements as
929   in Fig. 2h, but with 5 mM Mg-ATP. Means and SD of three independent experiments.

930

931
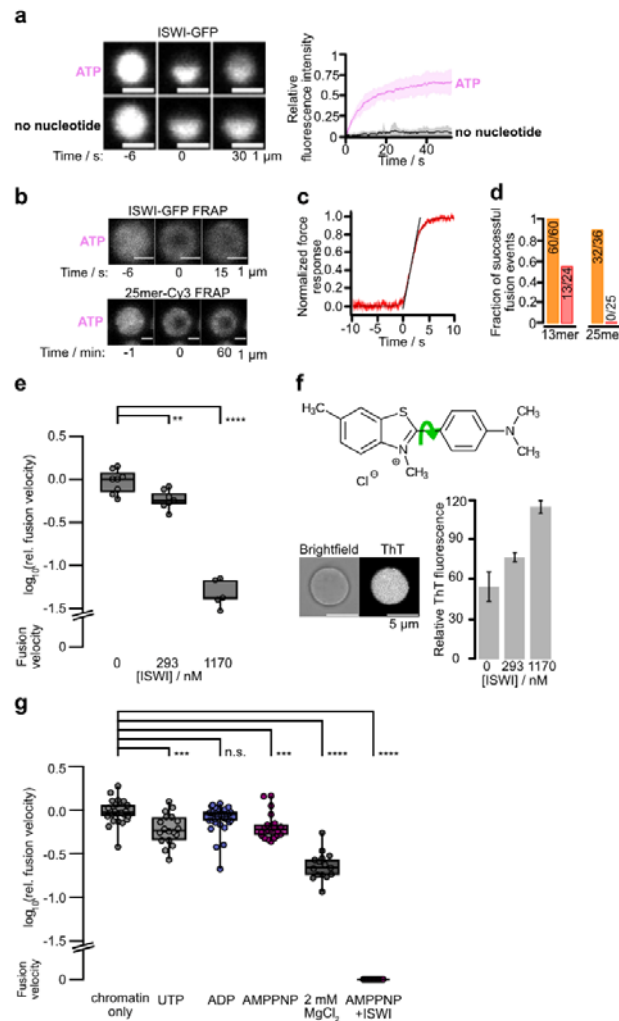
Figure S3. a, Intra-condensate mobility of ISWI-GFP measured by partial-condensate FRAP. Half of a condensate was bleached in presence and absence of Mg-ATP (1 mM). Line is an average and shadow SD of 15 bleached condensates for each condition. **b,** ISWI-GFP is more mobile than chromatin in condensates. Dual FRAP of ISWI-GFP and Cy3-labeled condensates formed by 25mer arrays in presence of Mg-ATP (1 mM) and ISWI (100 nM). Independent replicates show similar results. **c,** Force readout of optical traps during controlled condensate fusion. The fusion velocity was determined as the slope of the tangent fitted to the normalized force data at the inflection point of the fitted function. Incurred forces during fusion are on the order of 1 pN (see Methods). **d,** Fraction of successful fusion events in 1 mM $MgCl_2$ (orange) and 5 mM $MgCl_2$ (red). Total nucleosome concentration was 1170 nM. **e,** Fusion between condensates measured by optical tweezers containing indicated ISWI concentrations and 1170 nM nucleosomes. Velocities were estimated as illustrated in Fig. S3c. Box plots show means and 25th/75th percentiles, whiskers the 9th and 91st percentiles. **f,** ISWI increased viscosity of condensates as reported by enhanced fluorescence of the molecular rotor thioflavin T (ThT). In a high viscosity medium, rotation around the C-C bond (green arrow) is constrained, and the excitation energy is released as fluorescence. Bars are average ThT fluorescence intensities relative to the outside medium; error: SD. Six condensates were analyzed for no ISWI and

948 293 nM ISWI, five for 1170 nM ISWI. **g,** Fusion between condensates without ISWI measured by optical
949 tweezers. Nucleotides and free Mg^{2+} show only modest effects on fusion velocity.
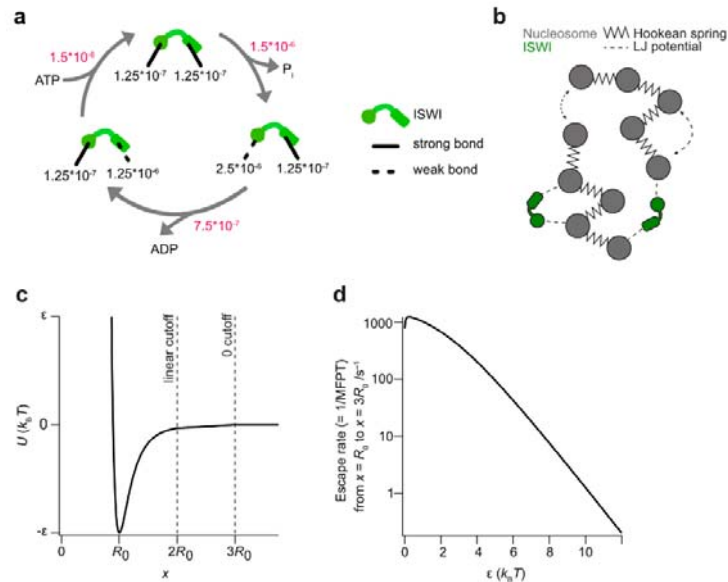
950

951 **Figure S4. a,** A model for the independent switching of the strengths of the two nucleosome
952 interaction sites during ISWI´s ATPase cycle. Escape rates (black) and transition rates (red) in timestep^{-}
953 ^{1} are indicated. **b,** Schematic representation of the implementation of the model in Fig. 4a for
954 molecular dynamics simulations. **c,** Modified Lennard-Jones potential used in simulations. Below
955 distances of $2R_0$ a regular Lennard-Jones potential is used. Between $2R_0$ and $3R_0$ the potential is
956 described using a linear approximation, while interactions with range above $3R_0$ are set to 0. **d,**
957 Conversion of the strength of the modified Lennard-Jones potential to escape rates based on the mean
958 first passage time of potential escape (Gray & Yong, 2021).

959 **Movie S1. FLIM-FRET timelapse with ATP**

960 **Movie S2. FLIM-FRET timelapse with AMPPNP**

961 **Movie S3. Controlled fusion with optical tweezers of chromatin condensates containing ISWI and**
962 **ADP-BeF$_x$**

963 **Movie S4. Controlled fusion with optical tweezers of chromatin condensates containing ISWI and**
964 **ATP**

965 **Movie S5. Simulation of ISWI FRAP with graph**

966 **Movie S6. Simulation of condensate fusion with graph**

967 **Table S1. Oligonucleotide list**

Name	Sequence (5'->3')	Description
oFMP839	GCTTGCATGCCTGCAGGTCG	To PCR ON60 fragment used for ATPase assay
oFMP864	CTGGAGAATCCCGGTGCCG	To PCR ON60 fragment used for ATPase assay and 0N60-EcoRI fragment used for FLIM-FRET
oFMP1260	TAAGCAGAATTCGCTTGCATGCCTGCAGGTCG	To PCR [atto647N]0N60-EcoRI fragment used for FLIM-FRET
oFMP1261	[ATTO647N]CTGGAGAATCCCGGTGCCG	To PCR [atto647N]0N60-EcoRI fragment used for FLIM-FRET and 0N60-EcoRI fragment used for FLIM-FRET

968

969 **References**

970 Adhireksan, Z., Sharma, D., Lee, P. L. & Davey, C. A. (2020). Near-atomic resolution structures of interdigitated nucleosome fibres. *Nature Communations*. https://doi.org/10.1038/s41467-020-18533-2

973 Beaudouin, J., Mora-Bermúdez, F., Klee, T., Daigle, N. & Ellenberg, J. (2006). Dissecting the contribution of diffusion and interactions to the mobility of nuclear proteins. *Biophysical Journal*, *90*(6), 1878–1894. https://doi.org/10.1529/BIOPHYSJ.105.071241

976 Bell, O., Schwaiger, M., Oakeley, E. J., Lienert, F., Beisel, C., Stadler, M. B. & Schübeler, D. (2010). *Accessibility of the Drosophila genome discriminates PcG repression, H4K16 acetylation and replication timing*. https://doi.org/10.1038/nsmb.1825

979 Bhardwaj, S. K., Hailu, S. G., Olufemi, L., Brahma, S., Kundu, S., Hota, S. K., Persinger, J. & Bartholomew, B. (2020). Dinucleosome specificity and allosteric switch of the ISW1a ATP-dependent chromatin

981   remodeler in transcription regulation. *Nature Communications*.

982   https://doi.org/10.1038/s41467-020-19700-1

983   Blosser, T. R., Yang, J. G., Stone, M. D., Narlikar, G. J. & Zhuang, X. (2009). Dynamics of nucleosome

984   remodelling by individual ACF complexes. *Nature*, *462*, 1022–1027.

985   https://doi.org/10.1038/nature08627

986   Boyer, L. A., Logie, C., Bonte, E., Becker, P. B., Wade, P. A., Wolffe, A. P., Wu, C., Imbalzano, A. N. &

987   Peterson, C. L. (2000). Functional delineation of three groups of the ATP-dependent family of

988   chromatin remodeling enzymes. *Journal of Biological Chemistry*, *275*(25), 18864–18870.

989   https://doi.org/10.1074/jbc.M002810200

990   Burak, Y., Ariel, G. & Andelman, D. (2003). Onset of DNA aggregation in presence of monovalent and

991   multivalent counterions. *Biophysical Journal*, *85*(4), 2100–2110. https://doi.org/10.1016/S0006-

992   3495(03)74638-4

993   Clapier, C. R., v Corona, D. F., Becker, P. B., Nightingale, K. P. & Programme, I. (2001). Critical Role for

994   the Histone H4 N Terminus in Nucleosome Remodeling by ISWI. *MOLECULAR AND CELLULAR*

995   *BIOLOGY*, *21*(3), 875–883. https://doi.org/10.1128/MCB.21.3.875-883.2001

996   Clapier, C. R., Verma, N., Parnell, T. J. & Cairns, B. R. (2020). Cancer-Associated Gain-of-Function

997   Mutations Activate a SWI/SNF-Family Regulatory Hub. *Molecular Cell*, *80*(4), 712-725.e5.

998   https://doi.org/10.1016/J.MOLCEL.2020.09.024

999   Corona, D. F. V., Längst, G., Clapier, C. R., Bonte, E. J., Ferrari, S., Tamkun, J. W. & Becker, P. B. (1999).

1000   ISWI is an ATP-dependent nucleosome remodeling factor. *Molecular Cell*, *3*(2), 239–245.

1001   https://doi.org/10.1016/S1097-2765(00)80314-7

1002 Dann, geoffrey P., Liszczak, glen P., Bagert, J. D., Müller, M. M., Nguyen, uyen, Wojcik, F., Brown, Z. Z.,

1003   Bos, J., Panchenko, tatyana, Pihl, R., Pollock, samuel B., Diehl, K. L., David allis, C. & Muir, tom W.

1004   (2017). *ISWI chromatin remodellers sense nucleosome modifications to determine substrate*

1005   *preference*. https://doi.org/10.1038/nature23671

1006 Deindl, S., Hwang, W. L., Hota, S. K., Blosser, T. R., Prasad, P., Bartholomew, B. & Zhuang, X. (2013).

1007   ISWI Remodelers Slide Nucleosomes with Coordinated Multi-Base-Pair Entry Steps and Single-

1008   Base-Pair Exit Steps. *Cell*, *152*(3), 442–452. https://doi.org/10.1016/J.CELL.2012.12.040

1009 Demeler, B. & Gorbet, G. E. (2016). Analytical Ultracentrifugation Data Analysis with UltraScan-III. In

1010   S. Uchiyama, F. Arisaka, W. Stafford & T. (eds.) Laue (Eds.), *Analytical Ultracentrifugation* (pp.

1011   119–143). Springer.

1012 Digman, M. A., Caiolfa, V. R., Zamai, M. & Gratton, E. (2008). The phasor approach to fluorescence

1013   lifetime imaging analysis. *Biophysical Journal*, *94*(2), 14–16.

1014   https://doi.org/10.1529/biophysj.107.120154

1015 Ditlev, J. A., Case, L. B. & Rosen, M. K. (2018). Who's In and Who's Out—Compositional Control of

1016   Biomolecular Condensates. *Journal of Molecular Biology*, *430*(23), 4666–4684.

1017   https://doi.org/10.1016/j.jmb.2018.08.003

1018 Elfring, L. K., Daniel, C., Papoulas, O., Deuring, R., Sarte, M., Moseley, S., Beek, S. J., Waldrip, W. R.,

1019   Daubresse, G., DePace, A., Kennison, J. A. & Tamkun, J. W. (1998). Genetic analysis of brahma:

1020   The drosophila homolog of the yeast chromatin remodeling factor SWI2/SNF2. *Genetics*, *148*(1),

1021   251–265. https://doi.org/10.1093/genetics/148.1.251

1022 Erdel, F., Baum, M. & Rippe, K. (2015). The viscoelastic properties of chromatin and the nucleoplasm

1023   revealed by scale-dependent protein mobility. *Journal of Physics: Condensed Matter*, *27*(6),

1024   064115. https://doi.org/10.1088/0953-8984/27/6/064115

1025   Erdel, F., Rademacher, A., Vlijm, R., Tünnermann, J., Frank, L., Weinmann, R., Schweigert, E.,

1026   Yserentant, K., Hummert, J., Bauer, C., Schumacher, S., al Alwash, A., Normand, C., Herten, D. P.,

1027   Engelhardt, J. & Rippe, K. (2020). Mouse Heterochromatin Adopts Digital Compaction States

1028   without Showing Hallmarks of HP1-Driven Liquid-Liquid Phase Separation. *Molecular Cell*, *78*(2),

1029   236-249.e7. https://doi.org/10.1016/j.molcel.2020.02.005

1030   Erdel, F. & Rippe, K. (2018). Formation of Chromatin Subcompartments by Phase Separation.

1031   *Biophysical Journal*, *114*(10), 2262–2270. https://doi.org/10.1016/j.bpj.2018.03.011

1032   Erdel, F., Schubert, T., Marth, C., Längst, G. & Rippe, K. (2010). Human ISWI chromatin-remodeling

1033   complexes sample nucleosomes via transient binding reactions and become immobilized at

1034   active sites. *Proceedings of the National Academy of Sciences of the United States of America*,

1035   *107*(46), 19873–19878. https://doi.org/10.1073/pnas.1003438107

1036   Finch, J. T. & Klug, A. (1976). Solenoidal model for superstructure in chromatin. *Proceedings of the*

1037   *National Academy of Sciences of the United States of America*, *73*(6), 1897.

1038   https://doi.org/10.1073/PNAS.73.6.1897

1039   Gamarra, N., Johnson, S. L., Trnka, M. J., Burlingame, A. L. & Narlikar, G. J. (2018). The nucleosomal

1040   acidic patch relieves auto-inhibition by the ISWI remodeler SNF2h. *ELife*, *7*.

1041   https://doi.org/10.7554/eLife.35322

1042   Gelbart, M. E., Bachman, N., Delrow, J., Boeke, J. D. & Tsukiyama, T. (2005). Genome-wide

1043   identification of Isw2 chromatin-remodeling targets by localization of a catalytically inactive

1044   mutant. *Genes & Development*, *19*(8), 942. https://doi.org/10.1101/GAD.1298905

1045   Gibson, B. A., Blaukopf, C., Lou, T., Chen, L., Doolittle, L. K., Finkelstein, I., Narlikar, G. J., Gerlich, D. W.

1046   & Rosen, M. K. (2023). In diverse conditions, intrinsic chromatin condensates have liquid-like

1047   material properties. *Proceedings of the National Academy of Sciences of the United States of*

1048   *America*, *120*(18). https://doi.org/10.1073/PNAS.2218085120

1049 Gibson, B. A., Doolittle, L. K., Schneider, M. W. G., Jensen, L. E., Gamarra, N., Henry, L., Gerlich, D. W.,

1050   Redding, S. & Rosen, M. K. (2019). Organization of Chromatin by Intrinsic and Regulated Phase

1051   Separation. *Cell*, *179*(2), 470-484.e21. https://doi.org/10.1016/j.cell.2019.08.037

1052 Goins, A. B., Sanabria, H. & Waxham, M. N. (2008). Macromolecular crowding and size effects on probe

1053   microviscosity. *Biophysical Journal*, *95*(11), 5362–5373.

1054   https://doi.org/10.1529/BIOPHYSJ.108.131250

1055 Gray, T. H. & Yong, E. H. (2021). An effective one-dimensional approach to calculating mean first

1056   passage time in multi-dimensional potentials. *The Journal of Chemical Physics*, *154*(8), 084103.

1057   https://doi.org/10.1063/5.0040071

1058 Grüne, T., Brzeski, J., Eberharter, A., Clapier, C. R., Corona, D. F. V., Becker, P. B. & Müller, C. W. (2003).

1059   Crystal structure and functional analysis of a nucleosome recognition module of the remodeling

1060   factor ISWI. *Molecular Cell*, *12*(2), 449–460. https://doi.org/10.1016/S1097-2765(03)00273-9

1061 Hagerman, T. A., Fu, Q., Molinié, B., Denvir, J., Lindsay, S. & Georgel, P. T. (2009). Chromatin stability

1062   at low concentration depends on histone octamer saturation levels. *Biophysical Journal*, *96*(5),

1063   1944–1951. https://doi.org/10.1016/j.bpj.2008.10.070

1064 Hamiche, A., Sandaltzopoulos, R., Gdula, D. A. & Wu, C. (1999). ATP-dependent histone octamer sliding

1065   mediated by the chromatin remodeling complex NURF. *Cell*, *97*(7), 833–842.

1066   https://doi.org/10.1016/S0092-8674(00)80796-5

1067 Harrer, N., Schindler, C. E. M., Bruetzel, L. K., Forné, I., Ludwigsen, J., Imhof, A., Zacharias, M., Lipfert,

1068   J. & Mueller-Planitz, F. (2018). Structural Architecture of the Nucleosome Remodeler ISWI

1069   Determined from Cross-Linking, Mass Spectrometry, SAXS, and Modeling. *Structure*, *26*(2), 282–

1070   294.e6. https://doi.org/10.1016/J.STR.2017.12.015

1071 Hihara, S., Pack, C. G., Kaizu, K., Tani, T., Hanafusa, T., Nozaki, T., Takemoto, S., Yoshimi, T., Yokota, H.,

1072   Imamoto, N., Sako, Y., Kinjo, M., Takahashi, K., Nagai, T. & Maeshima, K. (2012). Local

1073   Nucleosome Dynamics Facilitate Chromatin Accessibility in Living Mammalian Cells. *Cell Reports*,

1074   *2*(6), 1645–1656. https://doi.org/10.1016/j.celrep.2012.11.008

1075 Hodges, H. C., Stanton, B. Z., Cermakova, K., Chang, C. Y., Miller, E. L., Kirkland, J. G., Ku, W. L., Veverka,

1076   V., Zhao, K. & Crabtree, G. R. (2018). Dominant-negative SMARCA4 mutants alter the accessibility

1077   landscape of tissue-unrestricted enhancers. *Nature Structural and Molecular Biology*, *25*(1), 61–

1078   72. https://doi.org/10.1038/s41594-017-0007-3

1079 Hsieh, T. H. S., Weiner, A., Lajoie, B., Dekker, J., Friedman, N. & Rando, O. J. (2015). Mapping

1080   nucleosome resolution chromosome folding in yeast by Micro-C. *Cell*, *162*(1), 108.

1081   https://doi.org/10.1016/J.CELL.2015.05.048

1082 Kagalwala, M. N., Glaus, B. J., Dang, W., Zofall, M. & Bartholomew, B. (2004). Topography of the ISW2-

1083   nucleosome complex: Insights into nucleosome spacing and chromatin remodeling. *EMBO*

1084   *Journal*, *23*(10), 2092–2104. https://doi.org/10.1038/sj.emboj.7600220

1085 Keizer, V. I. P., Grosse-Holz, S., Woringer, M., Zambon, L., Aizel, K., Bongaerts, M., Delille, F., Kolar-

1086   Znika, L., Scolari, V. F., Hoffmann, S., Banigan, E. J., Mirny, L. A., Dahan, M., Fachinetti, D. &

1087   Coulon, A. (2022). Live-cell micromanipulation of a genomic locus reveals interphase chromatin

1088   mechanics.   *Science*,   *377*(6605),   489–495.

1089   https://doi.org/10.1126/SCIENCE.ABI9810/SUPPL_FILE/SCIENCE.ABI9810_MDAR_REPRODUCIBI

1090   LITY_CHECKLIST.PDF

1091   Kim, J. M., Visanpattanasin, P., Jou, V., Liu, S., Tang, X., Zheng, Q., Li, K. Y., Snedeker, J., Lavis, L. D.,

1092   Lionnet, T. & Wu, C. (2021). Single-molecule imaging of chromatin remodelers reveals role of

1093   atpase in promoting fast kinetics of target search and dissociation from chromatin. *ELife*, *10*.

1094   https://doi.org/10.7554/eLife.69387

1095   Klinker, H., Haas, C., Harrer, N., Becker, P. B. & Mueller-Planitz, F. (2014). Rapid purification of

1096   recombinant histones. *PLoS ONE*, *9*(8). https://doi.org/10.1371/JOURNAL.PONE.0104029

1097   Klinker, H., Mueller-Planitz, F., Yang, R., Forné, I., Liu, C. F., Nordenskiöld, L. & Becker, P. B. (2014).

1098   ISWI remodelling of physiological chromatin fibres acetylated at lysine 16 of histone H4. *PLoS*

1099   *ONE*, *9*(2). https://doi.org/10.1371/journal.pone.0088411

1100   Korber, P. & Becker, P. B. (2010). Nucleosome dynamics and epigenetic stability. *Essays in*

1101   *Biochemistry*, *48*, 63–74. https://doi.org/10.1042/BSE0480063

1102   Kornberg, R. D. & Lorch, Y. (2020). Primary Role of the Nucleosome. *Molecular Cell*, *79*(3), 371–375.

1103   https://doi.org/10.1016/J.MOLCEL.2020.07.020

1104   Koulouras, G., Panagopoulos, A., Rapsomaniki, M. A., Giakoumakis, N. N., Taraviras, S. & Lygerou, Z.

1105   (2018). EasyFRAP-web: a web-based tool for the analysis of fluorescence recovery after

1106   photobleaching data. *Nucleic Acids Research*, *46*, 467–472. https://doi.org/10.1093/nar/gky508

1107   Kroschwald, S., Munder, M. C., Maharana, S., Franzmann, T. M., Richter, D., Ruer, M., Hyman, A. A. &

1108   Alberti, S. (2018). Different Material States of Pub1 Condensates Define Distinct Modes of Stress

1109   Adaptation   and   Recovery.   *Cell   Reports*,   *23*(11),   3327–3339.

1110   https://doi.org/10.1016/J.CELREP.2018.05.041

1111   Längst, G., Bonte, E. J., Corona, D. F. V. & Becker, P. B. (1999). Nucleosome movement by CHRAC and

1112   ISWI without disruption or trans-displacement of the histone octamer. *Cell*, *97*(7), 843–852.

1113   https://doi.org/10.1016/S0092-8674(00)80797-7

1114   Larson, A. G. & Narlikar, G. J. (2018). The Role of Phase Separation in Heterochromatin Formation,

1115   Function,   and   Regulation.   *Biochemistry*,   *57*(17),   2540–2548.

1116   https://doi.org/10.1021/acs.biochem.8b00401

1117   Leonard, J. D. & Narlikar, G. J. (2015). A Nucleotide-Driven Switch Regulates Flanking DNA Length

1118   Sensing   by   a   Dimeric   Chromatin   Remodeler.   *Molecular   Cell*,   *57*(5),   850–859.

1119   https://doi.org/10.1016/J.MOLCEL.2015.01.008

1120   Li, L., Chen, K., Sia, Y., Hu, P., Ye, Y. & Chen, Z. (2023). Structure of the ISW1a complex bound to the

1121   dinucleosome. *BioRxiv* . https://doi.org/10.1101/2023.01.02.522444

1122   Li, W., Hu, J., Shi, B., Palomba, F., Digman, M. A., Gratton, E. & Jiang, H. (2020). Biophysical properties

1123   of AKAP95 protein condensates regulate splicing and tumorigenesis. *Nature Cell Biology*, *22*(8),

1124   960–972. https://doi.org/10.1038/s41556-020-0550-8

1125   Logie, C., Tse, C., Hansen, J. C. & Peterson, C. L. (1999). The Core Histone N-Terminal Domains Are

1126   Required for Multiple Rounds of Catalytic Chromatin Remodeling by the SWI/SNF and RSC

1127   Complexes†. *Biochemistry*, *38*(8), 2514–2522. https://doi.org/10.1021/BI982109D

1128   Ludwigsen, J., Hepp, N., Klinker, H., Pfennig, S. & Mueller-Planitz, F. (2018). Remodeling and

1129   repositioning of nucleosomes in nucleosomal arrays. In *Methods in Molecular Biology*.

1130   https://doi.org/10.1007/978-1-4939-8556-2_18

1131   Ludwigsen, J., Klinker, H. & Mueller-Planitz, F. (2013). No need for a power stroke in ISWI-mediated

1132   nucleosome sliding. *EMBO Reports*, *14*(12), 1092–1097.

1133   https://doi.org/10.1038/EMBOR.2013.160

1134   Maeshima, K., Iida, S. & Tamura, S. (2021). *Physical Nature of Chromatin in the Nucleus*.

1135   https://doi.org/10.1101/cshperspect.a040675

1136   Maeshima, K., Matsuda, T., Shindo, Y., Imamura, H., Tamura, S., Imai, R., Kawakami, S., Nagashima, R.,

1137   Soga, T., Noji, H., Oka, K. & Nagai, T. (2018). A Transient Rise in Free Mg2+ Ions Released from

1138   ATP-Mg Hydrolysis Contributes to Mitotic Chromosome Condensation. *Current Biology*, *28*(3),

1139   444-451.e6. https://doi.org/10.1016/j.cub.2017.12.035

1140   Maeshima, K., Rogge, R., Tamura, S., Joti, Y., Hikima, T., Szerlong, H., Krause, C., Herman, J., Seidel, E.,

1141   DeLuca, J., Ishikawa, T. & Hansen, J. C. (2016). Nucleosomal arrays self-assemble into

1142   supramolecular globular structures lacking 30-nm fibers. *The EMBO Journal*, *35*(10), 1115–1132.

1143   https://doi.org/10.15252/EMBJ.201592660

1144   Mueller-Planitz, F., Klinker, H., Ludwigsen, J. & Becker, P. B. (2013). The ATPase domain of ISWI is an

1145   autonomous nucleosome remodeling machine. *Nature Structural and Molecular Biology*.

1146   https://doi.org/10.1038/nsmb.2457

1147   Munder, M. C., Midtvedt, D., Franzmann, T., Nüske, E., Otto, O., Herbig, M., Ulbricht, E., Müller, P.,

1148   Taubenberger, A., Maharana, S., Malinovska, L., Richter, D., Guck, J., Zaburdaev, V. & Alberti, S.

1149   (2016). A pH-driven transition of the cytoplasm from a fluid- to a solid-like state promotes entry

1150   into dormancy. *ELife*, *5*(MARCH2016). https://doi.org/10.7554/ELIFE.09347

1151   Muzzopappa, F., Hertzog, M. & Erdel, F. (2021). DNA length tunes the fluidity of DNA-based

1152   condensates. *Biophysical Journal*, *120*(7), 1288–1300.

1153   https://doi.org/10.1016/J.BPJ.2021.02.027

1154   Olins, A. L. & Olins, D. E. (1974). Spheroid chromatin units (v bodies). *Science*, *183*(4122), 330–332.

1155   https://doi.org/10.1126/science.183.4122.330

1156   Oppikofer, M., Bai, T., Gan, Y., Haley, B., Liu, P., Sandoval, W., Ciferri, C. & Cochran, A. G. (2017).

1157   Expansion of the ISWI chromatin remodeler family with new active complexes. *EMBO Reports*,

1158   *18*(10), 1697–1706. https://doi.org/10.15252/EMBR.201744011

1159   Ou, H. D., Phan, S., Deerinck, T. J., Thor, A., Ellisman, M. H. & O'Shea, C. C. (2017). ChromEMT:

1160   Visualizing 3D chromatin structure and compaction in interphase and mitotic cells. *Science*,

1161   *357*(6349). https://doi.org/10.1126/science.aag0025

1162   Pédelacq, J.-D., Cabantous, S., Tran, T., Terwilliger, T. C. & Waldo, G. S. (2006). *Engineering and*

1163   *characterization of a superfolder green fluorescent protein*. https://doi.org/10.1038/nbt1172

1164   Peeples, W. & Rosen, M. K. (2021). Mechanistic dissection of increased enzymatic rate in a phase-

1165   separated compartment. *Nature Chemical Biology*. https://doi.org/10.1038/s41589-021-00801-

1166   x

1167   Poirier, M. G., Bussiek, M., Langowski, J. & Widom, J. (2008). Spontaneous Access to DNA Target Sites

1168   in Folded Chromatin Fibers. *Journal of Molecular Biology*, *379*(4), 772–786.

1169   https://doi.org/10.1016/j.jmb.2008.04.025

1170   Poirier, M. G., Oh, E., Tims, H. S. & Widom, J. (2009). Dynamics and function of compact nucleosome

1171   arrays. *Nature Structural and Molecular Biology*, *16*(9), 938–944.

1172   https://doi.org/10.1038/nsmb.1650

1173   Post, C. B. & Zimm, B. H. (1982). Theory of DNA condensation: Collapse versus aggregation.

1174   *Biopolymers*, *21*(11), 2123–2137. https://doi.org/10.1002/BIP.360211104

1175   R Core Team. (2022). *R: A Language and Environment for Statistical Computing* (4.2.1). R Foundation

1176   for Statistical Computing.

1177   Ricci, M. A., Manzo, C., García-Parajo, M. F., Lakadamyali, M. & Cosma, M. P. (2015). Chromatin fibers

1178   are formed by heterogeneous groups of nucleosomes in vivo. *Cell*, *160*(6), 1145–1158.

1179   https://doi.org/10.1016/J.CELL.2015.01.054

1180   Rudolph, J., Mahadevan, J., Dyer, P. & Luger, K. (2018). Poly(ADP-ribose) polymerase 1 searches DNA

1181   via a 'monkey bar' mechanism. *ELife*, *7*. https://doi.org/10.7554/ELIFE.37818

1182   Schalch, T., Duda, S., Sargent, D. F. & Richmond, T. J. (2005). X-ray structure of a tetranucleosome and

1183   its implications for the chromatin fibre. *Nature 2005 436:7047*, *436*(7047), 138–141.

1184   https://doi.org/10.1038/nature03686

1185   Schindelin, J., Arganda-Carreras, I., Frise, E., Kaynig, V., Longair, M., Pietzsch, T., Preibisch, S., Rueden,

1186   C., Saalfeld, S., Schmid, B., Tinevez, J. Y., White, D. J., Hartenstein, V., Eliceiri, K., Tomancak, P. &

1187   Cardona, A. (2012). Fiji: an open-source platform for biological-image analysis. *Nature Methods*,

1188   *9*(7), 676–682. https://doi.org/10.1038/NMETH.2019

1189   Schneider, M. W. G., Gibson, B. A., Otsuka, S., Spicer, M. F. D., Petrovic, M., Blaukopf, C., Langer, C. C.

1190   H., Batty, P., Nagaraju, T., Doolittle, L. K., Rosen, M. K. & Gerlich, D. W. (2022). A mitotic

1191   chromatin phase transition prevents perforation by microtubules. *Nature*, *609*, 183.

1192   https://doi.org/10.1038/s41586-022-05027-y

1193   Schram, R. D., Klinker, H., Becker, P. B. & Schiessel, H. (2015). Computational study of remodeling in a

1194   nucleosomal array. *European Physical Journal E*, *38*(8). https://doi.org/10.1140/epje/i2015-

1195   15085-4

1196   Schuck, P. (2000). Size-distribution analysis of macromolecules by sedimentation velocity

1197   ultracentrifugation and Lamm equation modeling. *Biophysical Journal*, *78*(3), 1606–1619.

1198   https://doi.org/10.1016/S0006-3495(00)76713-0

1199   Shi, B., Li, W., Song, Y., Wang, Z., Ju, R., Ulman, A., Hu, J., Palomba, F., Zhao, Y., Le, J. P., Jarrard, W.,

1200   Dimoff, D., Digman, M. A., Gratton, E., Zang, C. & Jiang, H. (2021). UTX condensation underlies

1201   its tumour-suppressive activity. *Nature*, *597*(7878), 726–731. https://doi.org/10.1038/s41586-

1202   021-03903-7

1203   Strickfaden, H., Tolsma, T. O., Sharma, A., Underhill, D. A., Hansen, J. C. & Hendzel, M. J. (2020).

1204   Condensed Chromatin Behaves like a Solid on the Mesoscale In Vitro and in Living Cells. *Cell*,

1205   *183*(7), 1772-1784.e13. https://doi.org/10.1016/J.CELL.2020.11.027

1206   Tilly, B. C., Chalkley, G. E., van der Knaap, J. A., Moshkin, Y. M., Kan, T. W., Dekkers, D. H. W., Demmers,

1207   J. A. A. & Peter Verrijzer, C. (2021). In vivo analysis reveals that ATP-hydrolysis couples

1208   remodeling to SWI/SNF release from chromatin. *ELife*, *10*. https://doi.org/10.7554/eLife.69424

1209   Verschure, P. J., van der Kraan, I., Manders, E. M. M., Hoogstraten, D., Houtsmuller, A. B. & van Driel,

1210   R. (2003). Condensed chromatin domains in the mammalian nucleus are accessible to large

1211   macromolecules. *EMBO Reports*, *4*(9), 861–866. https://doi.org/10.1038/sj.embor.embor922

1212   Wang, J., Choi, J. M., Holehouse, A. S., Lee, H. O., Zhang, X., Jahnel, M., Maharana, S., Lemaitre, R.,

1213   Pozniakovsky, A., Drechsel, D., Poser, I., Pappu, R. v., Alberti, S. & Hyman, A. A. (2018). A

1214   Molecular Grammar Governing the Driving Forces for Phase Separation of Prion-like RNA Binding

1215   Proteins. *Cell*, *174*(3), 688-699.e16. https://doi.org/10.1016/j.cell.2018.06.006

1216   Weidemann, T., Wachsmuth, M., Knoch, T. A., Müller, G., Waldeck, W. & Langowski, J. (2003).

1217   Counting nucleosomes in living cells with a combination of fluorescence correlation spectroscopy

1218   and   confocal   imaging.   *Journal   of   Molecular   Biology*,   *334*(2),   229–240.

1219   https://doi.org/10.1016/j.jmb.2003.08.063

1220   Whitehouse, I., Rando, O. J., Delrow, J. & Tsukiyama, T. (2007). Chromatin remodelling at promoters

1221   suppresses   antisense   transcription.   *Nature*,   *450*(7172),   1031–1035.

1222   https://doi.org/10.1038/nature06391

1223   Woodcock, C. L. F. (1973). Ultrastructure of inactive chromatin. *Journal of Cell Biology*, *59*, A368.

1224   Yamada, K., Frouws, T. D., Angst, B., Fitzgerald, D. J., Deluca, C., Schimmele, K., Sargent, D. F. &

1225   Richmond, T. J. (2011). Structure and mechanism of the chromatin remodelling factor ISW1a.

1226   *Nature*. https://doi.org/10.1038/nature09947

1227   Yang, J. G., Madrid, T. S., Sevastopoulos, E. & Narlikar, G. J. (2006). The chromatin-remodeling enzyme

1228   ACF is an ATP-dependent DNA length sensor that regulates nucleosome spacing. *Nature*

1229   *Structural and Molecular Biology*, *13*(12), 1078–1083. https://doi.org/10.1038/nsmb1170

1230   Yang, J. G. & Narlikar, G. J. (2007). FRET-based methods to study ATP-dependent changes in chromatin

1231   structure. *Methods*, *41*(3), 291–295. https://doi.org/10.1016/j.ymeth.2006.08.015

1232   Zhang, M., Díaz-Celis, C., Onoa, B., Cañari-Chumpitaz, C., Requejo, K. I., Liu, J., Vien, M., Nogales, E.,

1233   Ren, G. & Bustamante, C. (2022). Molecular Organization of the Early Stages of Nucleosome

1234   Phase Separation Visualized by Cryo-Electron Tomography. *Molecular Cell*, *82*(16), 3000.

1235   https://doi.org/10.1016/J.MOLCEL.2022.06.032

1236   Zhang, Y., Narlikar, G. J. & Kutateladze, T. G. (2021). Enzymatic Reactions inside Biological

1237   Condensates. *Journal of Molecular Biology*, *433*(12). https://doi.org/10.1016/j.jmb.2020.08.009

1238